Morphogen gradients are regulated by porous media characteristics of the developing tissue

Justina Stark[1,2,3,§], Rohit Krishnan Harish[1,4,5,*], Ivo F. Sbalzarini[1,2,3,5,†], Michael Brand[1,4,5,†,§]

[1]Technische Universität Dresden, Faculty of Computer Science, Germany.
[2]Max Planck Institute of Molecular Cell Biology and Genetics, Dresden, Germany.
[3]Center for Systems Biology Dresden, Dresden, Germany.
[4]Center for Regenerative Therapies Dresden, Dresden, Germany.
[5]Cluster of Excellence Physics of Life, Dresden, Germany.
*Present address: Institute of Science and Technology Austria, Am Campus 1, 3400 Klosterneuburg, Austria.
†These authors share senior authorship.
§Corresponding authors (jstark@mpi-cbg.de, michael.brand@tu-dresden.de)

Abstract

Long-range morphogen gradients have been proposed to form by morphogen diffusion from a localized source to distributed sinks in the target tissue. The role of complex embryo geometries in this process is less well understood and ignored by most mathematical models. We address this by numerically reconstructing pore-scale 3D geometries of zebrafish embryos during epiboly from light-sheet microscopy images. In these high-resolution 3D geometries, we simulate Fgf8a gradient formation. The simulations show that when realistic embryo geometries are considered, a source-diffusion-degradation mechanism with additional binding to polymers of the extracellular matrix (HSPG) is sufficient to explain self-organized emergence and robust maintenance of Fgf8a gradients. The predicted normalized gradient is robust against changes in source and sink rates but sensitive to changes in the pore connectivity of the extracellular space, demonstrating the importance of considering realistic geometries when studying morphogen gradients.

Keywords: Complex geometry, Multiscale modeling, Gradient robustness, Zebrafish epiboly, Fibroblast growth factor, GPU-accelerated simulation

1 Introduction

The global body plan governing cell differentiation and tissue morphogenesis during embryonic development is defined by graded concentration fields of morphogens. Morphogens are signaling molecules, mostly proteins, are secreted by localized source cells and move through the embryo toward their target tissue, where they are degraded. Different modes of morphogen transport have been proposed, including diffusion, transcytosis, and directed transport via cytonemes [73, 117].

The simplest and most common mode of morphogen transport is by diffusion through the embryonic extracellular space (ECS). The ECS is the complex-shaped interstitial space between the cells, which resembles a porous medium [76, 77]. When circumventing obstacles in tortuous porous media, molecules have to move further on average to reach the same mean square displacement as in free space, leading to reduced effective diffusivity [8, 12, 13, 15, 25, 31, 73, 98, 105]. Moreover, some parts of a porous medium may be inaccessible due to imperfect pore connectivity [44], compartmentalizing the space. Before morphogens diffuse through the ECS, they are secreted by cells. Finally, cells take up extracellular morphogens by endocytosis.

Both morphogen secretion and uptake amount to surface reactions, which depend on the surface area and accessibility of the cell surfaces. Pore accessibility and volume further influence bulk reactions [113]. Together, this results in a complex interplay of surface reactions, volume diffusion, and ECS geometry, as illustrated in Fig. 1.

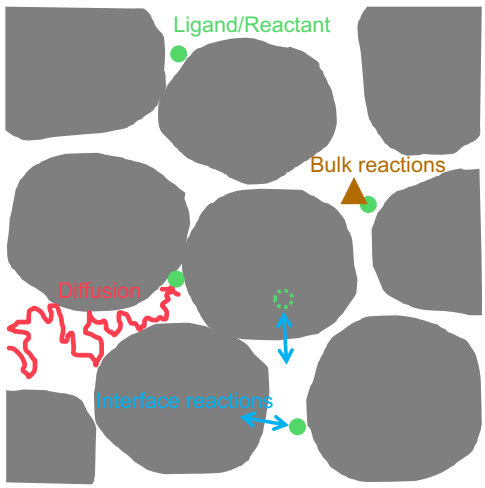

Figure 1: Schematic representation of diffusion in a porous medium with bulk and surface reactions. The tortuosity and imperfect connectivity of the pore-scale geometry lowers the effective diffusivity and compartmentalize the space. Interfacial reactions depend on pore-surface area and pore accessibility.

Therefore, extracellular morphogen transport can be expected to significantly depend on ECS geometry [98], and the effective morphogen-receptor binding rate can be significantly smaller than the intrinsic rate and depend on the effective diffusivity [88, 118]. Diffusive hindrance, domain compartmentalization, and receptor localization hence influence morphogen gradient formation and maintenance in porous ECS geometries [58, 73, 112, 123].

Another important factor modulating morphogen gradient formation is the transient binding of morphogens to non-receptors in the ECS, such as heparan sulfate proteoglycans (HSPGs) [4, 33, 57, 94, 109, 119]. HSPGs are tethered to cell membranes by a transmembrane core protein and have long poly-disaccharides reaching into the ECS, with heparan sulfate (HS) chains to which morphogens bind. HSPG binding has several effects on the morphogen gradient: in the ECS, it slows down morphogen diffusion while protecting morphogens from degradation by proteases [92]. At the cell membrane, it mediates complex formation with the morphogen receptor, locally enriching morphogens near cell surfaces. Concentrating morphogen diffusion to the cell surfaces and preventing morphogen loss and degradation in the ECS, HSPG binding stabilizes long-range gradients [38, 94, 119, 122]. All of these interactions add to the geometry influence and are subsumed in the *porous media characteristics* of the ECS.

A morphogen that forms long-range concentration gradients is Fibroblast growth factor 8a (Fgf8a). As a member of the highly conserved Fgf family, Fgf8a is involved in maintaining the midbrain-hindbrain boundary, somitogenesis, limb induction, and tissue patterning in zebrafish [26, 70, 89, 102]. During zebrafish epiboly, it forms a gradient along the animal-vegetal (AV) axis [40, 122].

Epiboly is the first morphogenetic movement in zebrafish during embryogenesis. It starts $\approx$4 hours post fertilization (hpf) when actomyosin contraction in the yolk syncytial layer (YSL)

pulls the enveloping layer (EVL) towards the vegetal pole [17], as depicted in Fig. 2. This causes the blastoderm, consisting of the EVL and a deep-cell layer (DCL), to thin and spread over the yolk until completely engulfing the yolk by the end of epiboly [17].

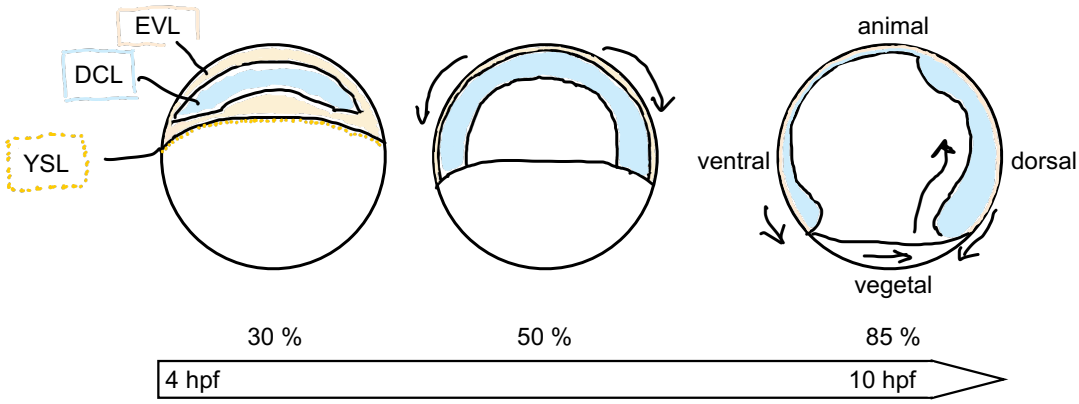

Figure 2: Illustration of zebrafish epiboly. Representative stages at around 40, 50, and 85% epiboly with deep-cell layer (DCL, blue), enveloping layer (EVL, yellow), and yolk syncytial layer (YSL, yellow dots). Starting at around 4 hpf (40% epiboly), the yolk moves toward the animal pole, and the blastoderm, composed of EVL, DCL, and YSL, starts spreading over the yolk. Toward the end of epiboly, the blastoderm almost completely engulfs the yolk, and asymmetry along the dorsal-ventral axis emerges.

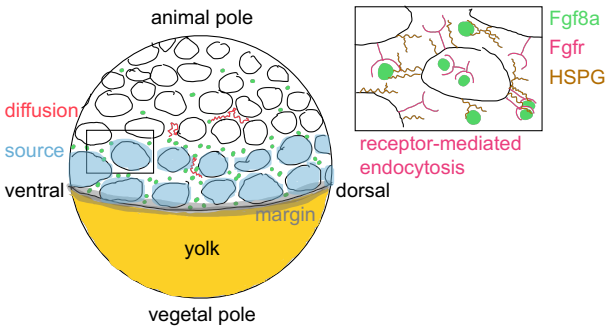

Figure 3: Scheme of Fgf8a gradient formation during zebrafish epiboly. Secreted by source cells at the blastoderm margin (blue), Fgf8a diffuses along tortuous paths through the ECS, further hindered by HSPG binding. The complex formation of Fgf8a, HSPG, and Fgf-receptors initiates internalization and endocytosis of Fgf8a into target cells acting as sinks.

During this dynamic cell movement, Fgf8a is secreted by a band of cells at the blastoderm margin, from where it diffuses throughout the ECS [40, 101, 122], as schematically illustrated in Fig. 3. Interaction with HSPG at the cell surfaces and in the ECS is assumed to stabilize Fgf8a gradients by protecting Fgf8a from degradation and by slowing down its diffusion [38, 40, 122]. Cell-surface HSPGs also enhance Fgf8a binding to its receptors, Fgfr1 and Fgfr4, in the target tissue [38]. It is assumed that the internalized complex consists of Fgf8a, Fgfr, and HS in a 2:2:2 stoichiometry [78, 100]. Complex internalization involves clathrin-mediated endocytosis. Together, these processes—secretion, diffusion, degradation, and endocytosis—amount to a source-diffusion-degradation (SDD) [37, 52] mechanism with additional HSPG binding [40, 122].

Whether this SDD mechanism is sufficient to explain the experimentally observed Fgf8a gradient, however, has not been shown so far. It is difficult if not impossible to measure *in vivo* the individual roles of source and sink rates, HSPG binding, diffusion coefficient, and ECS geometry. To disentangle these different factors and quantify how they modulate morphogen gradient formation individually and collectively, mathematical and numerical models are required.

Many mathematical models of morphogen gradient formation have been developed over the

decades [5, 6, 16, 22, 34, 58, 64, 68, 74, 88]. Most of them, however, neglect the 3D porous geometry of the real embryo ECS. Some even simplify the diffusion space to a 2D disk or a 1D line. 1D models have been successfully used to study morphogen gradient robustness to different source sizes [23] and to the absence of a sink [20], to non-receptor binding [57], competition for receptor binding of two heparin-binding growth factors [33], scaling across different embryo sizes [34], and local accumulation times (LATs) for different source [7] and sink configurations [16], as well as tissue growth [120]. Thanks to their simplicity, 1D models are popular for studying the influence of a single factor at a time and for deriving analytical solutions of morphogen gradients.

Another way to simplify the system for deriving analytical solutions is through geometrical upscaling, i.e., collectively representing the tortuous diffusion paths by an effective average constant [50]. Numerical homogenization is a common upscaling technique, which has been used to model morphogen gradient formation in the cortical region of the embryonic *Drosophila* syncytium [93], enabling the derivation of an analytical mean-field expression for that system.

Numerical solutions of models allow going beyond simple geometries and enable incorporating experimental image data. Image-based models of embryonic development have been developed in 2D+time, e.g., to model limb growth and digit patterning during vertebrate development [11, 59, 66, 68, 75] and kidney branching morphogenesis [67], as well as in 3D+time to model mouse limb-bud growth [24].

These image-based geometries, however, consisted of a singly connected surface (or outline in the 2D models), differing considerably from the porous zebrafish ECS geometry with its many intricately shaped and disconnected surfaces. These ECS surfaces, mostly cell surfaces, play an important role in gradient formation by confining the diffusion space and localizing morphogen sources and sinks. Despite this significant role, the zebrafish ECS geometry has been simplified in models of morphogen gradient formation during epiboly to the arc of a circle [73, 122] or the surface of a sphere [61, 62].

Although simplified models are often well suited to test general principles of gradient formation, they cannot capture locally varying dynamics, heterogeneities, and zonation effects. They are also difficult to validate with *in vivo* data, which are acquired in the real geometry. A major difficulty is that various key parameters required for modeling morphogen gradient formation remain unknown because they are difficult or impossible to measure experimentally. These include morphogen production and degradation rates, receptor and non-receptor binding affinities and concentrations, and advection velocities due to growth. The models hence remain underdetermined with multiple unknown parameters, requiring parameter searches and fitting [107].

Even with all parameters known, the embryos' spatial complexity and temporal deformation pose challenges in modeling their realistic geometries. As embryo geometries cannot be mathematically parameterized, they require algorithmic representations at high resolution to capture pore-scale dynamics. In particular, morphogen gradient formation is a molecular process influenced by the ECS geometry across several orders of magnitude, from interstitial spaces (nanometers) to the embryo size (millimeters). Computational models that consider all length scales can be prohibitively expensive to compute. Memory-efficient algorithms, like geometry-adaptive sparse grids [47], and acceleration of the multi-scale simulation in Graphics Processing Units (GPUs) are thus required to render simulations in realistic embryo geometries feasible.

Here, we use a memory-efficient GPU-accelerated algorithm [110] to address the above bi-

ological questions by simulating Fgf8a gradient formation in realistic 3D ECS geometries of zebrafish epiboly derived from light-sheet microscopy volumes at the resolution of individual cells. In these image-based geometries, we simulate morphogen gradient formation by solving a system of coupled partial differential equations, accounting for the spatial variations of sources and sinks and the interaction of Fgf8a with HSPG. Using this image-based model, we quantify gradient robustness to changes in different factors, such as source and sink rates, HSPG binding, morphogen diffusivity, and ECS geometry.

We find that the normalized Fgf8a gradient is robust against changes in the source and sink rates, whereas it is sensitive to changes that affect diffusive hindrance. Besides changes in the molecular diffusion constant of the morphogen itself, the latter in particular includes changes in the extracellular HSPG concentration and changes to the ECS geometry. Concretely, peak concentrations near the source are more preserved, and the gradients are steeper and shorter for higher HSPG concentrations, lower diffusion coefficients, and higher ECS tortuosity.

2 Materials and Methods

We state the equations modeling Fgf8a gradient formation, discuss the numerical method and parallel computing software used to numerically solve these equations, and we describe image acquisition and image processing.

2.1 Model equations

As schematically illustrated in Fig. 3, Fgf8a gradient formation is explained by an SDD mechanism with HSPG binding [40, 122]. Specifically, two diffusing fractions of Fgf8a with different diffusion coefficients have been identified *in vivo*: a major fraction of ≈93 % moving freely with $D = 55\,\mu\mathrm{m}^2\mathrm{s}^{-1}$ and a HSPG-bound fraction of ≈7 % moving with $D = 4\,\mu\mathrm{m}^2\mathrm{s}^{-1}$ [40]. In addition to interacting with extracellular HSPG, Fgf8a binds to cell-surface HSPG, which mediates its receptor complex formation [38, 78, 100]. The cell-surface bound Fgf8a fraction is not detected by Fluorescence Correlation Spectroscopy (FCS) measurements in the ECS but by Heparinase (HepI) injection experiments, in which cleavage of the HS side chains has been shown to lead to an increase in overall Fgf8a concentrations detected by FCS [40].

We account for the different Fgf8a interactions by distinguishing four concentration fields in space and time: freely diffusing Fgf8a ([Fgf8a]), slowly diffusing HSPG-bound Fgf8a in the ECS ($[\mathrm{Fgf8a} : \mathrm{HSPG}^{\mathrm{ECS}}]$), immobile cell-surface HSPG-bound Fgf8a ($[\mathrm{Fgf8a} : \mathrm{HSPG}^{\mathrm{cellSurf}}]$), and the immobile ternary 2:2:2 complex of Fgf8a, Fgfr, and HSPG at the cell surface ($[\mathrm{Fgf8a}_2 : \mathrm{HSPG}_2^{\mathrm{cellSurf}} : \mathrm{Fgfr}_2]$). The biochemical kinetics between these species in the ECS is:

$$\mathrm{Fgf8a} + \mathrm{HSPG}^{\mathrm{ECS}} \underset{k_{\mathrm{off}}}{\overset{k_{\mathrm{on}}}{\rightleftharpoons}} \mathrm{Fgf8a} : \mathrm{HSPG}^{\mathrm{ECS}}\,, \tag{2.1.1}$$

at the cell surfaces, it is:

$$\mathrm{Fgf8a} + \mathrm{HSPG}^{\mathrm{cellSurf}} \underset{k_{\mathrm{off}}}{\overset{k_{\mathrm{on}}}{\rightleftharpoons}} \mathrm{Fgf8a} : \mathrm{HSPG}^{\mathrm{cellSurf}}\,, \tag{2.1.2}$$

and ternary receptor complex-formation occurs as:

$$2\,\mathrm{Fgf8a} : \mathrm{HSPG}^{\mathrm{cellSurf}} + 2\,\mathrm{Fgfr} \xrightarrow{k_{\mathrm{complex}}} \mathrm{Fgf8a}_2 : \mathrm{HSPG}_2^{\mathrm{cellSurf}} : \mathrm{Fgfr}_2\,, \tag{2.1.3}$$

where k_{on} and k_{off} are the association and dissociation rates of Fgf8a to HSPG, and k_{complex} is the association rate of the ternary $[\mathrm{Fgf8a}_2 : \mathrm{HSPG}_2^{\mathrm{cellSurf}} : \mathrm{Fgfr}_2]$ complex. As cell-surface HSPGs have been shown to trap Fgf8a and mediate receptor complex-formation and dimerization [38, 78], our model assumes that Fgf8a binding to $\mathrm{HSPG}^{\mathrm{cellSurf}}$ precedes complex formation. Further, the model combines complex association, dissociation, and dimerization into a single effective forward reaction to reduce the number of unknown rate constants.

Applying the principle of mass-action and assuming diffusive transport, these kinetics yield the following partial differential equations for the evolution of the four concentration fields in space $\boldsymbol{x}$ and time t:

$$\begin{aligned}\frac{\partial[\mathrm{Fgf8a}]}{\partial t} =& \nabla^2 D_{\mathrm{Fgf8a}}[\mathrm{Fgf8a}] \\ &+ f_{\mathrm{source}}(\boldsymbol{x}) \\ &- k_{\mathrm{on}}[\mathrm{Fgf8a}][\mathrm{HSPG}^{\mathrm{ECS}}] \\ &+ k_{\mathrm{off}}[\mathrm{Fgf8a} : \mathrm{HSPG}^{\mathrm{ECS}}] \\ &- k_{\mathrm{on}}[\mathrm{Fgf8a}][\mathrm{HSPG}^{\mathrm{cellSurf}}] \\ &+ k_{\mathrm{off}}[\mathrm{Fgf8a} : \mathrm{HSPG}^{\mathrm{cellSurf}}] \\ &- k_{\mathrm{decay}}[\mathrm{Fgf8a}]\end{aligned} \tag{2.1.4}$$

$$\begin{aligned}\frac{\partial[\mathrm{Fgf8a} : \mathrm{HSPG}^{\mathrm{ECS}}]}{\partial t} =& \nabla^2 D_{\mathrm{Fgf8a:HSPG}^{\mathrm{ECS}}}[\mathrm{Fgf8a} : \mathrm{HSPG}^{\mathrm{ECS}}] \\ &+ k_{\mathrm{on}}[\mathrm{Fgf8a}][\mathrm{HSPG}^{\mathrm{ECS}}] \\ &- k_{\mathrm{off}}[\mathrm{Fgf8a} : \mathrm{HSPG}^{\mathrm{ECS}}]\end{aligned} \tag{2.1.5}$$

$$\begin{aligned}\frac{\partial[\mathrm{Fgf8a} : \mathrm{HSPG}^{\mathrm{cellSurf}}]}{\partial t} =& k_{\mathrm{on}}[\mathrm{Fgf8a}][\mathrm{HSPG}^{\mathrm{cellSurf}}] \\ &- k_{\mathrm{off}}[\mathrm{Fgf8a} : \mathrm{HSPG}^{\mathrm{cellSurf}}] \\ &- 2k_{\mathrm{complex}}[\mathrm{Fgf8a} : \mathrm{HSPG}^{\mathrm{cellSurf}}]^2[\mathrm{Fgfr}]^2\end{aligned} \tag{2.1.6}$$

$$\begin{aligned}\frac{\partial[\mathrm{Fgf8a}_2 : \mathrm{HSPG}_2^{\mathrm{cellSurf}} : \mathrm{Fgfr}_2]}{\partial t} =& k_{\mathrm{complex}}[\mathrm{Fgf8a} : \mathrm{HSPG}^{\mathrm{cellSurf}}]^2[\mathrm{Fgfr}]^2 \\ &- k_{\mathrm{internalize}}[\mathrm{Fgf8a}_2 : \mathrm{HSPG}_2^{\mathrm{cellSurf}} : \mathrm{Fgfr}_2]\,.\end{aligned} \tag{2.1.7}$$

D_{Fgf8a} and $D_{\mathrm{Fgf8a:HSPG}^{\mathrm{ECS}}}$ are the diffusion coefficients of the free and HSPG-bound Fgfa8 fractions in the ECS, respectively. $[\mathrm{HSPG}^{\mathrm{ECS}}]$ and $[\mathrm{HSPG}^{\mathrm{cellSurf}}]$ are the HSPG concentrations with free binding sites in the ECS and at the cell surfaces, respectively. The rate k_{decay} describes the decay of free Fgf8a in the ECS through thermal denaturation and proteolysis [53, 92]. The rate $k_{\mathrm{internalize}}$ is the complex internalization rate through endocytosis. The model assumes that for each internalized complex, two new Fgfr and $\mathrm{HSPG}^{\mathrm{cellSurf}}$ appear at the cell membrane, respectively, i.e., that their total concentration is constant over time. This simplifies the more

complicated real receptor fate, of which Fgfr4 has been shown to be mainly recycled, whereas Fgfr1 with ligand is mainly degraded in the lysosome [42]. Fgf8a secretion by source cells is represented by the source term $f_{\text{source}}(\boldsymbol{x})$.

Fgf8a sources and sinks vary in space. Concretely, only the deep cells participate in Fgf8a production and uptake, i.e., there is no production and uptake in the YSL and EVL (see Fig. 2). We denote ECS boundaries that belong to either the EVL or YSL by $\partial\Omega_{\text{shell}}$, such that the surfaces of the deep cells are defined by $\partial\Omega_{\text{ECS}}\backslash\partial\Omega_{\text{shell}}$. Within the deep cells, we further spatially restrict the source to a band of cells near the blastoderm margin. We define the width of this cell band w_{source} and its distance from the margin d_{margin}, so that we can mathematically formalize the source term as

$$f_{\text{source}}(\boldsymbol{x}) = \begin{cases} k_{\text{source}} & \text{for} \quad \boldsymbol{x} \in \partial\Omega_{\text{ECS}}\backslash\partial\Omega_{\text{shell}},\, 0 \leq d_{\text{margin}}(\boldsymbol{x}) \leq w_{\text{source}} \\ 0 & \text{otherwise} \end{cases} \tag{2.1.8}$$

with source rate k_{source}.

In addition to Fgf8a molecular degradation with rate k_{decay} everywhere in the ECS, ternary complex formation and subsequent endocytic uptake constitutes an additional Fgf8a sink $f_{\text{sink}}(\boldsymbol{x})$. This endocytic sink is localized only to the deep cell surfaces $\partial\Omega_{\text{ECS}}\backslash\partial\Omega_{\text{shell}}$ by setting [Fgfr] to zero everywhere else. We model $f_{\text{sink}}(\boldsymbol{x})$ as a first-order reaction with rate $k_{\text{internalize}}$

$$f_{\text{sink}}(\boldsymbol{x}, t) = \begin{cases} k_{\text{internalize}}[\text{Fgf8a}_2 : \text{HSPG}_2^{\text{cellSurf}} : \text{Fgfr}_2](\boldsymbol{x}, t) & \text{for} \quad \boldsymbol{x} \in \partial\Omega_{\text{ECS}}\backslash\partial\Omega_{\text{shell}} \\ 0 & \text{otherwise}\,. \end{cases} \tag{2.1.9}$$

2.2 Numerical method

To numerically model localized sources and sinks and solve Eq. (2.1.4)–(2.1.7) in pore-scale 3D ECS geometries derived from images, we use an open-source image-based simulation pipeline for reaction-diffusion processes in porous media [110]. This pipeline computes a level-set representation of the diffusion domain based on volumetric microscopy images or microcomputed tomography scans. Based on the level-set function, it generates geometry-adapted sparse grids on which it solves inhomogeneous reaction-diffusion partial differential equations with multi-GPU acceleration. A detailed explanation of the numerical method has been given by Stark and Sbalzarini (2023).

The pipeline addresses the high memory requirements of multi-scale models using geometry-adapted sparse grids [47], enabling individual point allocation in any domain subspace as needed. As sparse grids preserve the Cartesian neighborhood of a structured grid, they enable fast neighborhood access and differential operator approximation using standard grid-based schemes. Sparse grids are, therefore, suitable for discretizing porous media geometries in a memory- and compute-efficient way.

Generating such a geometry-adapted sparse grid for the complex-shaped geometry of an embryonic ECS diffusion domain Ω requires a numerical description of its boundary $\partial\Omega$ embedded in the grid, i.e., the interface between Ω and the surrounding space S. We use the level-set method [79, 111] to implicitly represent $\partial\Omega$ as the zero-level set of a higher-dimensional function

ϕ. Specifically, we use the signed-distance function (SDF):

$$\phi_{\mathrm{SDF}}(\boldsymbol{x}) = \begin{cases} +d & \text{for} \quad \boldsymbol{x} \in \Omega \\ -d & \text{for} \quad \boldsymbol{x} \in S \backslash \Omega \\ \ \ 0 & \text{for} \quad \boldsymbol{x} \in \partial\Omega\,, \end{cases} \tag{2.2.1}$$

which is smooth around the surface $\partial\Omega$ and provides geometric information through the orthogonal distance d of any point $\boldsymbol{x}$ in the domain to the closest point on the nearest surface.

We compute ϕ_{SDF} by first generating a binary pixel mask of the ECS from the image using the pixel-classification tool ilastik [9]. This represents is the indicator function for Ω. Using this indicator function, we initialize $\phi(\boldsymbol{x}, 0)$ with +1 inside Ω and -1 outside Ω. This serves as initial condition for computing ϕ_{SDF} using the classic Sussman level-set redistancing algorithm [111], which finds the SDF as the stationary solution of

$$\frac{\partial \phi(\boldsymbol{x}, \alpha)}{\partial \alpha} = \varsigma(\phi(\boldsymbol{x}, \alpha))(1 - |\boldsymbol{\nabla}\phi(\boldsymbol{x}, \alpha)|) \tag{2.2.2}$$

for large α. To prevent interface shifting across cell boundaries for steep ϕ, and to accelerate convergence of the iterations if ϕ is flat near the interface, the smoothed sign function σ is chosen as [81]:

$$\varsigma(\phi(\boldsymbol{x}, \alpha)) = \frac{\phi(\boldsymbol{x}, \alpha)}{\sqrt{\phi(\boldsymbol{x}, \alpha)^2 + |\boldsymbol{\nabla}\phi(\boldsymbol{x}, \alpha)|^2 h^2}}\,, \tag{2.2.3}$$

where h is the uniform grid spacing.

We perform Sussman redistancing with multi-CPU parallelization on a dense grid with first-order accuracy in space and time [110]. Using the so-computed ϕ_{SDF}, a geometry-adapted sparse grid containing only points in the diffusion domain is generated to reduce memory requirements. This sparse grid stores the four concentration fields along with ϕ_{SDF}. Together, this enables defining spatially varying diffusion coefficients and reaction rates, including surface reactions.

Taking advantage of the regular structure of sparse grids, the diffusion operators are discretized using finite-difference methods, which afford efficient memory access and parallelize well on multi-CPU and multi-GPU, in particular when an explicit time-stepping scheme is used [21, 51, 121]. Since we here consider a strongly memory-limited problem, we solve the model in time using the first-order explicit Euler time-stepping scheme, which does not require storing and communicating intermediate stages.

2.3 Software implementation

Even when using geometry-adapted sparse grids, the pore-scale models of the embryonic ECS exceed single-processor capacity by far, requiring efficient parallelization. We use the open-source C++ library OpenFPM for parallelizing the simulations [49]. OpenFPM data structures, which are generated at compile time using template meta-programming, hide communication from the application and are portable across CPU and GPU architectures [48].

OpenFPM implements distributed sparse block grids by dividing the domain into chunks of $8 \times 8 \times 8$ grid points and only allocating chunks containing at least one grid point [47]. This considerably reduces memory requirements for sparse geometries, such as the zebrafish ECS.

OpenFPM sparse grids are also multi-GPU accelerated, significantly reducing simulation times compared to simulations on multi-CPU [47]. These simulations have been shown to scale with problem size and number of GPUs for irregular porous media geometries [110]. In particular, it has been shown that the sparser the geometry and the locally denser the grid points, the larger the savings in memory and simulation run time [47, 110]. The zebrafish ECS has a particularly sparse geometry, occupying only ≈3% of 3D light-sheet microscopy volume, making it well-suited for OpenFPM sparse-grids discretization.

2.4 Acquisition of light-sheet microscopy time-lapse video

To geometrically characterize the zebrafish ECS and its boundaries, we collected Tg(bactin:hRas-EGFP) embryos, in which Enhanced Green Fluorescent Protein (EGFP) was targeted to the cell membrane. As the embryos reached the sphere stage, they were dechorionated and injected with 0.2 nL of a 5 µM solution of Tetramethylrhodamine (TMR)-labeled dextran at their animal pole, where ECS is abundant. As a hydrophilic polysaccharide, dextran does not cross the membrane barrier and distributes throughout the ECS as the embryo develops. This enabled us to track the ECS over the course of epiboly.

To perform multi-view imaging of embryos for 3D modeling, we used the Plan-Apochromat 20X/1.0W objective of the Zeiss light-sheet Z.1 microscope. For this, we first transferred the TMR-Dextran-injected embryos into a tube containing 1% low-melting point agarose, mixed with F-Z fluorescent microspheres at a 1:4000 dilution, stored at 42°C to prevent solidification. Together with the agarose–bead mix, the embryos (maximum three) were then sucked into a glass capillary (20 µL volume, 1 mm diameter) by pulling on the inserted plunger, such that the embryos were all spaced evenly inside the capillary. Once the agarose solidified, we transferred the capillary to a beaker containing E3 medium until the imaging chamber at the microscope was assembled. Thereafter, the capillary was inserted into the imaging chamber (also filled with E3), positioned, and automatically detected by imaging. An embryo embedded in the solidified agarose–bead mixture was then slowly pushed out of the capillary using the plunger until it reached the center of the detection volume.

Light-sheet adjustment, multi-view image-acquisition, and later multi-view reconstruction were performed according to the protocol detailed by Icha et al. [46] using the Fiji BigDataViewer plugin [83, 84]. Image acquisition was performed from five different angles over the course of epiboly. The resulting time-lapse multi-view image data set is composed of 25 frames of 3D image volumes acquired from 5 hpf (≈40% epiboly) to 9 hpf (≈90% epiboly) (voxel size = 0.4574 µm in all three dimensions, stack size: 1834×1739×1551 pixel). This allowed visualizing changes in the spatial arrangement of cells and the geometry of the ECS over the course of early development. Figure 4 shows exemplary z-slices of the video with the EGFP-hRas-labeled cell membranes in green and the TMR-Dextran-labeled ECS in magenta.

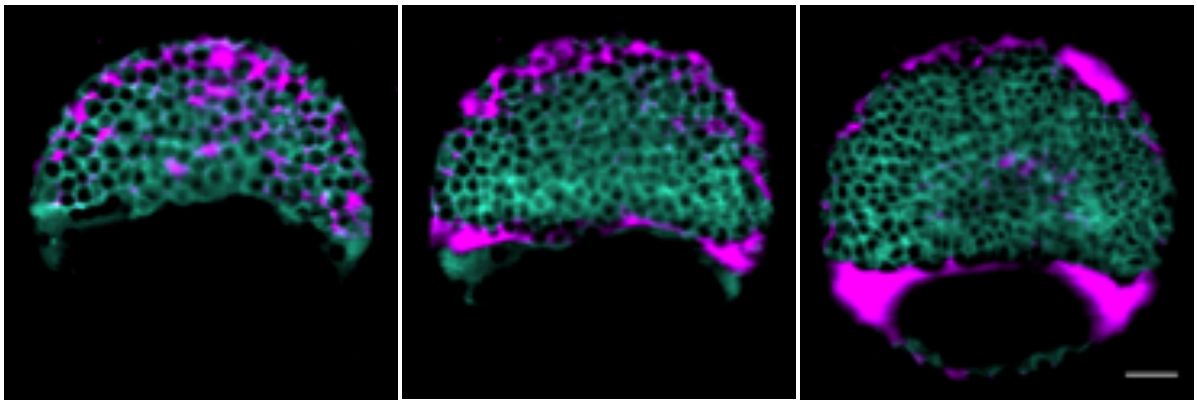

Figure 4: Light-sheet microscopy images of zebrafish epiboly. From left to right: exemplary optical sections from a Tg(bactin:hRas-EGFP) embryo at late blastula, early gastrula, and mid-gastrula stages, respectively, following image acquisition using a light-sheet fluorescence microscope and multi-view reconstruction. hRas-EGFP labels the cell membranes (green). ECS is marked by TMR-Dextran injection (magenta). Unidirectional views and single optical sections are shown for simplicity; scale bar: 50 µm.

2.5 Reconstructing 3D zebrafish ECS geometries based on light-sheet microscopy images

Using the TMR-dextran fluorescence signal of the light-sheet time-lapse video, we modeled ECS geometries using level-set sparse grids as explained in Sections 2.3 and 2.2. This image-based ECS reconstruction consisted of five steps, the intermediate results of which are shown in Fig. 5a–e for an exemplary z-slice. The steps were: 1) extracting volumes of individual time points from the light-sheet video; 2) image processing and segmentation using Fiji [99] and ilastik [9]; 3) processing of the segmentation result and conversion to an indicator function; 4) computing a numerical surface description as a signed distance function (SDF) using the level-set method; 5) generating a geometry-adapted discretization of the ECS using distributed sparse block grids [47]. We next describe these five image-based modeling steps in more detail.

The light-sheet video (exemplary z-slices in Fig. 4) was stored as a 0.7 TB HDF5 file containing five viewpoints plus their 3D fusion for all 25 time points. For geometry modeling the geometry, 3D fused views were extracted as separate files to reduce RAM/DRAM requirements. Extraction of the 3D multiview reconstruction of the TMR-dextran channel at each time point was done using the Multiview Reconstruction Tool from the Fiji BigDataViewer plugin [83, 84]. An exemplary z-slice is shown in Fig. 5a).

The resulting TIFF files were subsequently converted to the ilastik HDF5 file format using the ilastik Import/Export plugin in Fiji. In ilastik [9], the interactive Random Forest pixel classifier was used to obtain a pixel mask for the ECS. The classifier was trained by manual image example annotation for the two pixel classes, ECS versus non-ECS, where non-ECS included pixels of background, cells, and yolk. Pixel class annotation and prediction were repeated for different x, y, and z-slices of the 3D image volume at video time point 12 until the classification results no longer improved. The trained classifier was then used for pixel classification of the other 24 time points of the video without further manual annotation.

The segmentation result, shown in Fig. 5b for an exemplary z-slice, likely overestimates the ECS volume because ECS structures can be below pixel resolution. Nevertheless, the network character of the ECS geometry was successfully captured.

Postprocessing of the segmentation mask (pixel value of 2 in the ECS and 1 otherwise) was done before conversion to an indicator function. This included Gaussian filtering ($\sigma = 2$) and alignment of the sample rotation using the `scipy.ndimage` Python package [114]. Sample alignment made the margin plane horizontal (yellow dashed line in Fig. 5b and c) by rotation of the 3D pixel mask about the z-axis, applying the standard rotation matrix using trigonometric functions. The rotated mask was then interpolated back to the pixel grid using third-order spline interpolation. This was followed by thresholding the filtered and rotated segmentation mask, which was no longer binary, setting pixels to one with value > 1.4 and all others to -1. The threshold was determined such that it removes unconnected islands of size $\leq 3 \times 3 \times 3$ pixels, whose maximum value after Gaussian smoothing was 1.39 (examples marked by pink circles in Fig. 5b). This denoising step was necessary to avoid numerical instabilities in the Sussman algorithm that would otherwise be caused by imaging noise, at the expense of introducing a small bias and artificial smoothing of the ECS surface. This resulted in an indicator field as exemplary shown in Fig. 5c, which was stored as a binary file. Each of these binary files was 162.5 GB in size. The indicator function was then loaded onto a distributed-memory 3D computational grid on a compute cluster with multiple CPUs. Thin structures < 2 pixel in width were removed to fulfill the level-set resolution requirement resulting from the Nyquist-Shannon sampling theorem [110].

Finally, a representation of the ECS surfaces was computed as a SDF ϕ_{ECS}, as explained in Section 2.2. The exemplary result is shown in Fig. 5d. Based on this ϕ_{ECS}, a sparse block-grid representation of the ECS was generated, resulting in a memory-efficient geometry-adapted data structure as illustrated in Fig. 5e. A full 3D visualization of the resulting surface is shown in Fig. 6 for the time point at ≈60% epiboly. Following this procedure, we built models of the ECS geometries for all 25 time points of the light-sheet time-lapse video. Visualizations of the results at all time points are shown in Suppl. Fig. S8.

At full resolution, with one grid point per light-sheet microscopy voxel, representing the zebrafish ECS on a sparse block grid reduced memory requirements by a factor of 17, from ≈306 GB (dense grid, no blocks) to ≈17 GB (sparse block grid). This enables fully resolved numerical simulations on a GPU, since the sparse-grid data fits the DRAM of a typical GPU (here: Nvidia A100 with 40 GB DRAM). We further found that simulation results at full and half grid resolution were identical, indicating that the pixel resolution of the geometry was sufficient to yield grid-converged numerical results. Using half the resolution resulted in an overall 28-fold reduction in simulation times (from 110 hours to 4 hours of GPU compute time per run simulating 60 minutes of physical time). We therefore used a half-resolution computational grid (i.e., $h = 2$ pixel) in all simulations, resulting in a grid spacing of 0.92 µm and a memory requirement of 3.5 GB.

Using the numerical methods from Section 2.2, we solved the model equations from Section 2.1 in 3D ECS geometries at ≈40, 60, and 75% epiboly to study morphogen gradient emergence and maintenance.

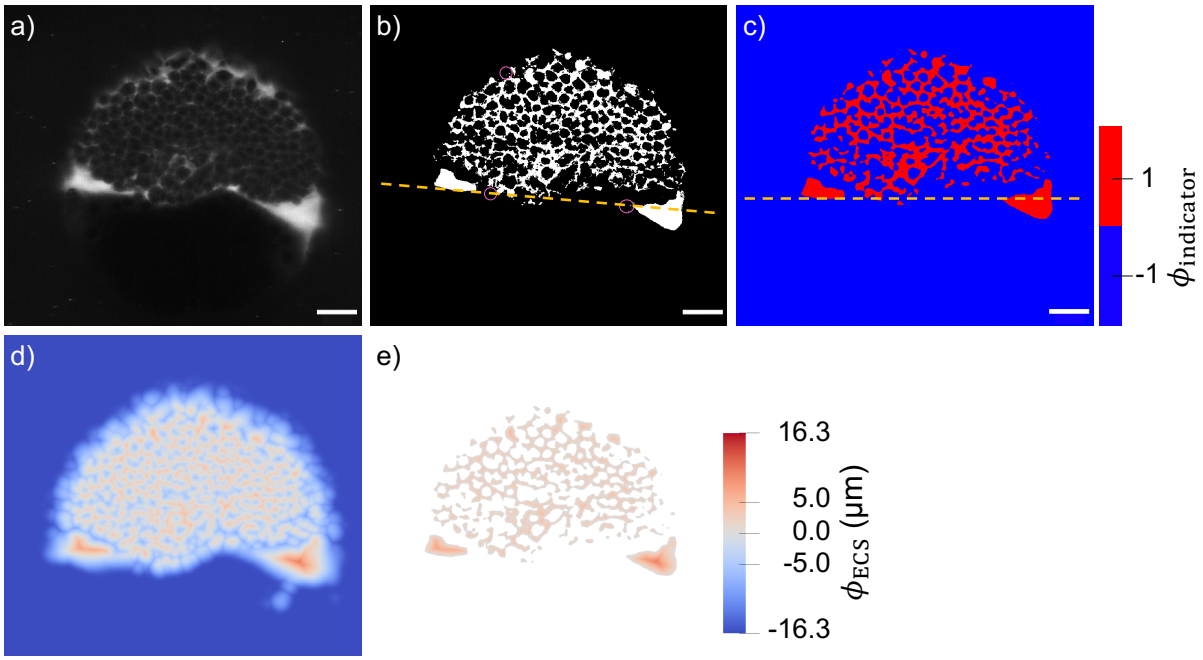

Figure 5: Steps for modeling ECS geometries from light-sheet microscopy volumes visualized for an exemplary time point (12 out of 25, ≈60 % epiboly) and z-slice (plane 480 from the epiblast in the direction of hypoblast and the yolk, i.e., the mid-plane formed by the AV/DV axes). (a) TMR-dextran channel of the light-sheet data after 3D multi-view fusion; fluorescence marks ECS. (b) Segmentation mask of the ECS (white) with a yellow dashed line showing the margin plane and pink circles highlighting specks of noise and small unconnected islands that were subsequently removed. (c) Binary indicator function of the ECS after mask denoising and horizontal alignment of the margin plane (yellow dashed line). (d) Redistanced signed-distance function ϕ_{ECS} of the level-set representation of the ECS surface. (e) Sparse block grid storing only points in the ECS; scale bars: 50 µm.

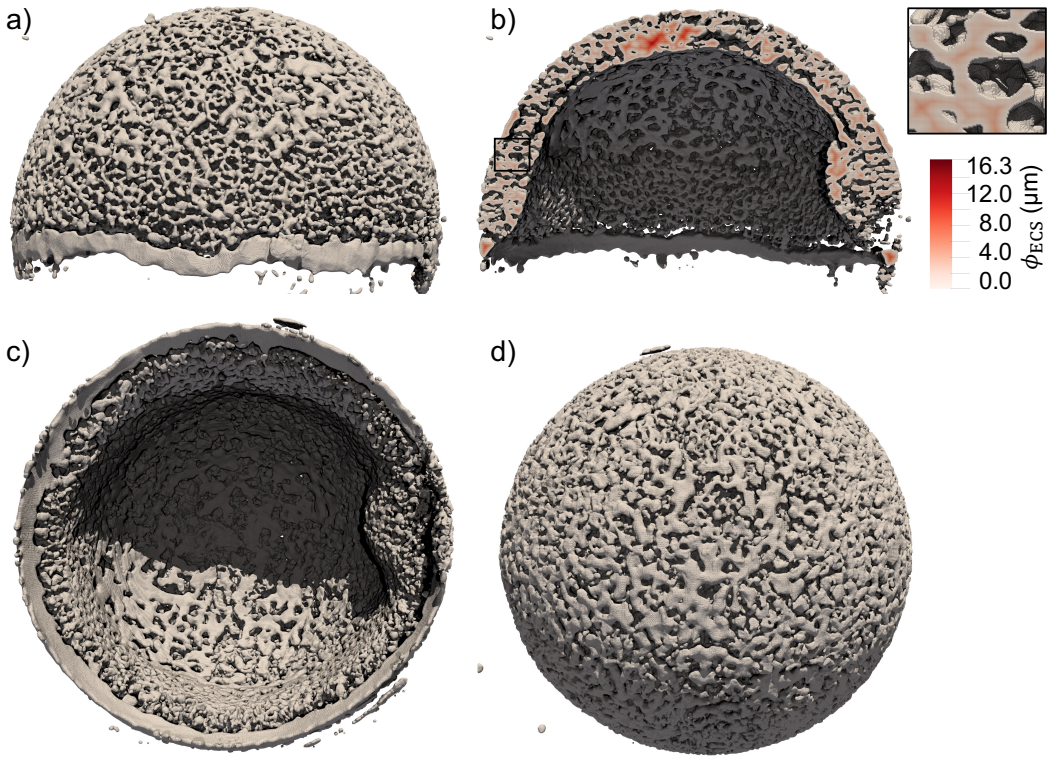

Figure 6: Visualization of the SDF representation of the ECS surface at ≈60% epiboly. We show an iso-surface rendering of $\phi_{\mathrm{ECS}} = 0$ in gray. (a) Side view oriented as in Fig. 4. (b) Cross-cut view with ϕ_{ECS} values in increasing distance to the ECS surface shown in shades of red (color bar). Face-on views from vegetal (c) and animal pole (d).

2.6 Modeling localized sources and sinks

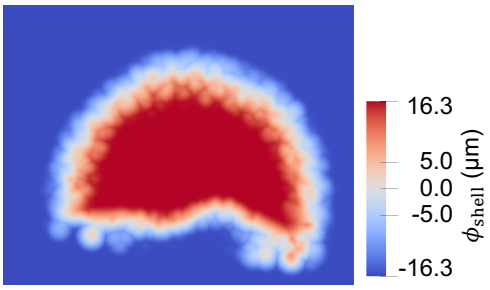

Figure 7: SDF of the embryo shell boundary, ϕ_{shell}, for an exemplary z-slice. Combining ϕ_{shell} (representing YSL and EVL boundaries) with ϕ_{ECS} enables restricting sources and sinks to the deep-cell surfaces.

In order to spatially restrict sources and sinks according to Eqs. (2.1.8) and (2.1.9) to the surfaces of the deep cells, these surfaces need to be distinguished from those of the YSL and EVL, i.e., what we call the *shell* boundary $\partial\Omega_{\text{shell}}$. To accomplish this, we computed another SDF, ϕ_{shell}, representing $\partial\Omega_{\text{shell}}$, following the procedure as described in Section 2.5, but using segmentation masks in which the cells have been blurred out by Gaussian filtering ($\sigma = 3$) followed by setting pixels to one whose value > 1.0 and all others to -1.

This resulted in a SDF as shown in Fig. 7. Combining ϕ_{shell} and ϕ_{ECS} enables defining the deep-cell surfaces as the set of grid points $p_{\boldsymbol{i}}^{\text{DCL}} \in \{p_1^{\text{DCL}}, \ldots, p_n^{\text{DCL}}\} = P^{\text{DCL}}$ within one grid spacing from $\partial\Omega_{\text{ECS}}$ and further than 15 µm away from $\partial\Omega_{\text{shell}}$, i.e., $P^{\text{DCL}} := \{\boldsymbol{i} \in \mathbb{N}^3 : 0 < \phi_{\text{ECS}}(\boldsymbol{x_i}) < h \text{ and } \phi_{\text{shell}} > 15\}$, to which we restrict [Fgfr] and [HSPG^{cellSurf}].

Fgf8a secretion was also restricted to this same set of grid points, additionally restricting the source location to a band of deep cells above the blastoderm margin [101]. The width of this band was ≈5 cells at early gastrula [40] and ≈8 cells at mid gastrula [101]. For this, w_{source} in Eq. (2.1.8) was set to 70 µm at 40 and 60% epiboly and to 112 µm at 70% epiboly, assuming an average cell diameter of 14 µm [40]. The model assumes that source cells also act as sink cells. Comparing the simulation results of this model with a model that assumes source cells to not act as sink, we found that the normalized gradient profiles are unaffected of this assumption (see Supplementary Note S3). The resulting sources and sinks of the model are visualized in Fig. 8 for an exemplary time point at ≈60% epiboly.

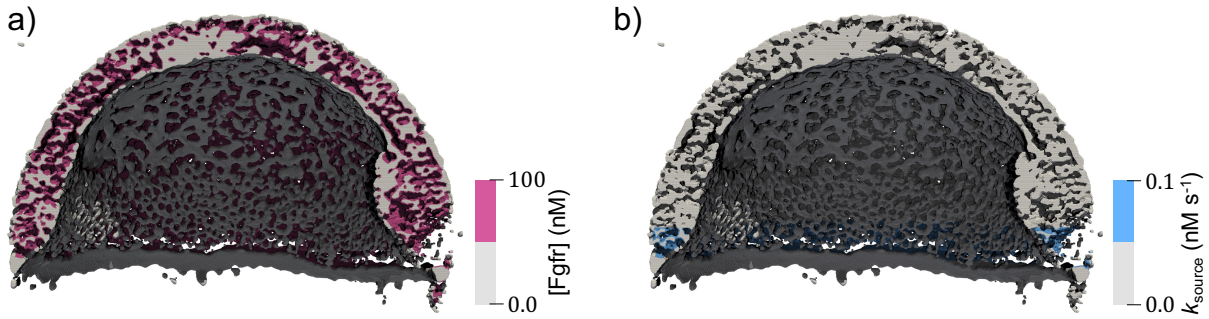

Figure 8: Spatially varying sources and sinks in the 3D model at an exemplary time point at ≈60% epiboly. Clipped model of the ECS showing that Fgf-receptors ((a) in pink) are restricted to the deep cell boundaries, i.e., not EVL nor YSL. The sources ((b) in blue) are restricted to ≈5 rows of deep cells above the margin of the blastoderm. Concentrations are given in units of nM, k_{source} in 1/s.

2.7 Parameter search

The model described in Eqs. (2.1.4)–(2.1.7) has several unknown parameters, including [Fgfr], [HSPG^{ECS}], [HSPG^{cellSurf}], k_{on}, k_{off}, k_{decay}, k_{complex}, $k_{\text{internalize}}$, and f_{source}. We performed a systematic parameter search to find values of the parameters that maintain the *in vivo* gradient.

Table 1: Summary of all model parameters. We combined literature values (references) with own experimental measurements ("Exp.") and deductive reasoning from known values as described in the text ("Text"). The remaining three parameters were determined in a computational parameter search ("Search").

Diffusion coefficients			
Fgf8a (93 % of extracellular Fgf8a)	D_{Fgf8a}	$55\,\mu\text{m}^2\text{s}^{-1}$	[40]
Fgf8a:HSPG (7 % of extracellular Fgf8a)	$D_{\text{Fgf8a:HSPG}^{\text{ECS}}}$	$4\,\mu\text{m}^2\text{s}^{-1}$	[40]
Concentrations			
maximal concentration of extracellular Fgf8a		7.9 nM	Exp.
extracellular HSPG concentration	[HSPG^{ECS}]	0.4 µM	Search
cell-surface HSPG concentration	[HSPG^{cellSurf}]	1.0 µM	Search
Fgf receptor concentration	[Fgfr]	0.1 µM	Text
On and off binding rates			
Association rate of Fgf8a and HSPG$^{\text{ECS/cellSurf}}$	k_{on}	$4.6 \times 10^{-6}\,(\text{nM}\,\text{s})^{-1}$	Text
Dissociation rate of Fgf8a and HSPG$^{\text{ECS/cellSurf}}$	k_{off}	$0.023\,\text{s}^{-1}$	[32, 108]
Dissociation constant of Fgf8a : HSPG$^{\text{ECS/cellSurf}}$	$K_{\text{D}}^{\text{Fgf8a:HSPG}}$	5.0 µM	[38], Text
Association rate of Fgf8a : HSPG^{cellSurf} and Fgfr	k_{complex}	$4.6 \cdot 10^{-5}\,(\text{nM}\,\text{s})^{-1}$	Text
Source and sink rates			
Fgf8a production rate	k_{source}	$0.1\,\text{nM}\,\text{s}^{-1}$	Search
Fgf8a molecular decay rate	k_{decay}	$1.3 \cdot 10^{-3}\,\text{s}^{-1}$	[122]
Internalization rate for Fgf8a$_2$: HSPG$_2^{\text{cellSurf}}$: Fgfr$_2$	$k_{\text{internalize}}$	$9 \cdot 10^{-3}\,\text{s}^{-1}$	Text

To maximize the predictive power of our model, we fixed as many parameters as possible to experimental or literature values, as summarized in Table 1. One of the unknown parameters is the overall binding and unbinding rate of Fgf8a to HSPG^{ECS} and HSPG^{cellSurf}. For the two HSPG families, glypican and syndecan, the dissociation constants, defined as $K_{\text{D}} = \frac{k_{\text{off}}}{k_{\text{on}}}$, of the Fgf8-HSPG interaction ($K_{\text{D}}^{\text{Fgf8-HSPG}}$) have been determined by *in vivo* dual-color fluorescence cross-correlation spectroscopy (FCCS) in the gastrulating zebrafish: $K_{\text{D}} = 1.03 \ldots 1.24\,\mu\text{M}$ (syndecans) and $K_{\text{D}} = 6.15 \pm 0.74\,\mu\text{M}$ (glypicans) [38]. Hence, both affinities are more than an order of magnitude lower than Fgf8-receptor binding affinities ($K_{\text{D}}^{\text{Fgf8a-Fgfr4}} = 46\,\text{nM}$ and $K_{\text{D}}^{\text{Fgf8a-Fgfr1}} = 100\,\text{nM}$ [90]).

Assuming that the syndecans and glypicans affinities are representative of the overall Fgf8a : HSPG interaction, and considering that more glypicans than syndecans are present in the zebrafish ECS [38], we set the dissociation constant of Fgf8a : HSPG^{ECS} and Fgf8a : HSPG^{cellSurf} in our model to an average $K_{\text{D}}^{\text{Fgf8a:HSPG}}$ of 5.0 µM. Using this $K_{\text{D}}^{\text{Fgf8a:HSPG}}$ and an HSPG unbinding rate $k_{\text{off}} = 0.023\,\text{s}^{-1}$, as has been measured for Fgf2 [32, 108], we find the binding rate $k_{\text{on}} = k_{\text{off}}/K_{\text{D}}^{\text{Fgf8a:HSPG}} = 4.6 \cdot 10^{-6}\,(\text{nM}\,\text{s})^{-1}$. Further, we assume a 10-times higher Fgfr binding rate of $k_{\text{complex}} = 4.6 \cdot 10^{-5}\,(\text{nM}\,\text{s})^{-1}$ and set [Fgfr] = 0.1 µM by approximating volume concentrations from experimentally determined Fgfr surface concentrations [90].

It has been experimentally shown that Fgf8a concentrations are higher at the membrane than in the ECS [38] and that cleavage of HS side-chains upon heparinase injection causes a two-fold increase in Fgf8a concentration levels in the ECS [40]. The exact factor by which [HSPG^{cellSurf}]

is higher than [HSPG^{ECS}] is, however, unknown, so we set it arbitrarily to $2\times$.

From the experimentally measured $k_{\mathrm{decay}} = 1.3 \cdot 10^{-3}\,\mathrm{s}^{-1}$ [122], and taking into account geometrical hindrance as discussed in Supplementary Note S5 and the gradient half-decay length λ from the *in vivo* gradient profile in Fig. 14, we estimate

$$k_{\mathrm{internalize}} = \frac{D_{\mathrm{Fgf8a}}}{\tau_{\mathrm{d}}\lambda^2} = \frac{55\,\mu\mathrm{m}^2\mathrm{s}^{-1}}{2.5 \cdot (50\,\mu\mathrm{m})^2} \approx 9 \cdot 10^{-3}\,\mathrm{s}^{-1}\,. \tag{2.7.1}$$

For the computational parameter search, we assumed that the experimentally measured intensity profile at 60% epiboly was at a steady state for this time point. We then searched for values of the remaining three parameters ("Search" in Table 1) that maintained this steady-state profile. For this, we initialized the Fgf8a concentration in the geometry reconstruction at 60% epiboly with the experimental profile shown in Fig. 9 as detailed in Supplementary Note S1. To compare the 3D simulation results with the 1D experimental gradient, we computed 1D profiles along the AV axis by averaging the sum of all four Fgf8a fractions in each xz-plane of the simulation grid. These concentration averages were subsequently normalized and plotted against the distance from the blastoderm margin, as shown in Fig. 10. Using the experimental profile as initial condition, we computed the solution of Eqs. (2.1.4)–(2.1.7) for different parameter sets until $t_{\max} = 60\,\mathrm{min}$, which was sufficiently long to ensure that gradients have reached a steady state.

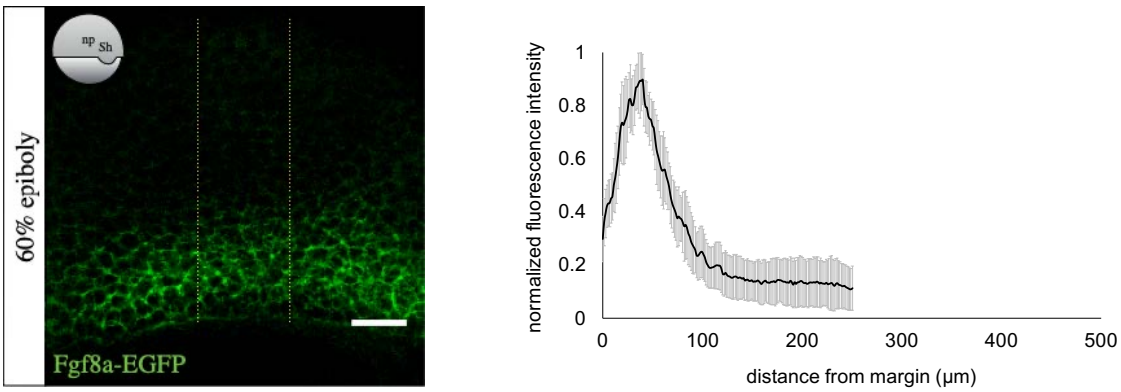

Figure 9: Experimentally measured Fgf8-EGFP gradient in the ECS at 60 % epiboly. The fluorescence intensity profile (right) is extracted from sum-intensity z-projected confocal images (left). Values are intensity averages across a 100 μm wide region (neural plate). Figure reproduced with permission from Harish et al. [40] *to do: ask journal for permission.* The embryo is oriented as in Fig. 3 and depicted in the inset (ventral left, dorsal right, animal pole top, vegetal pole bottom). Scale bar: 50 μm.

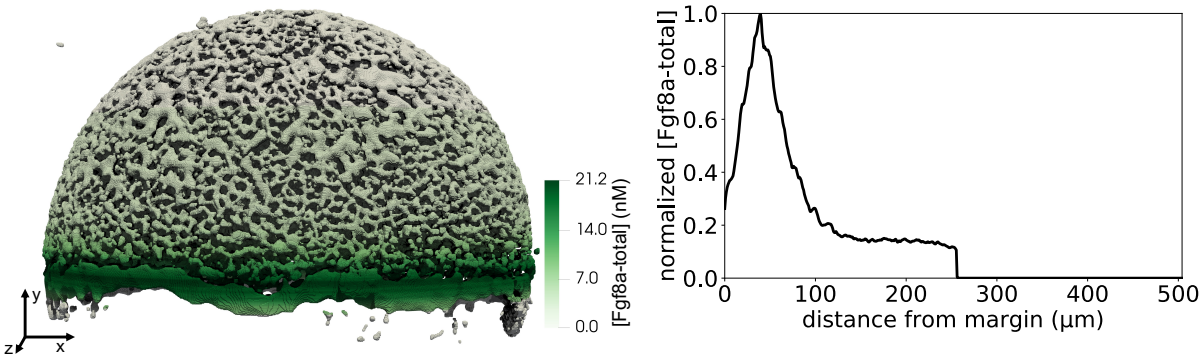

Figure 10: Initialization of the total Fgf8a concentration with the experimental fluorescence intensity profile from Fig. 9 at ≈60% epiboly. The concentration field in the simulation (left) was obtained by linearly interpolating between the discrete margin distances of the experimental profile and uniformly distributing the mass in each xz-plane. We converted normalized intensity values to concentrations by scaling with the maximum concentration measured by FCS. For comparison with experiments, we computed 1D profiles (right) along the AV axis by averaging the total Fgf8a concentration in each xz-plane. The model has the same orientation as the embryo in Fig. 9

With these assumptions, and using the experimental profile as initial condition, we tested different k_{source} and HSPG concentrations in simulations. These two parameters mainly influenced the Fgf8a / Fgf8a : HSPG^{ECS} ratio in the simulations, i.e., the higher [HSPG], the higher the bound fraction. We found that [HSPG^{ECS}] = 0.4 µM and [HSPG^{cellSurf}] = 1.0 µM closely matched the experimentally measured Fgf8a / Fgf8a : HSPG^{ECS} ratio (simulated ratio: 92.6% / 7.4%) after 60 minutes of simulated time, see Fig. 11b. For these parameter values, the concentration levels of the overall Fgf8a profile were well maintained when using a source rate of 0.1 nM s^{-1}, as shown in Fig. 11a.

Although maintaining the Fgf8a / Fgf8a : HSPG^{ECS} ratio and the overall profile, the simulated profile converges within 12 min to a steady state profile slightly flatter with a wider range than the experimental profile (Fig. 11a) and a lower peak concentration (see absolute concentration profiles in Suppl. Fig. S6). Possible explanations are that some of the parameter values is not correct, the experimental input profile is not at a steady state, or there is lower geometrical hindrance due to overestimated ECS connectivity and volume as a consequence of image-segmentation errors discussed in Section 2.5 and quantified in Section 3.2. Despite not perfectly maintaining the input profile's slope and range, the simulated profile maintains a drop close to the margin, likely caused by a zonation effect in the marginal region with low cell density and poor connectivity to the rest of the ECS (cf. Fig. 10). Furthermore, the normalized profiles maintain the overall shape of the *in vivo* gradient (Fig. 11a).

Overall, the parameters shown in Tab. 1 preserve the experimentally measured gradient at 60% epiboly and reproduce the *in vivo* ratio of Fgf8a / Fgf8a : HSPG^{ECS}. We use these parameters throughout the manuscript.

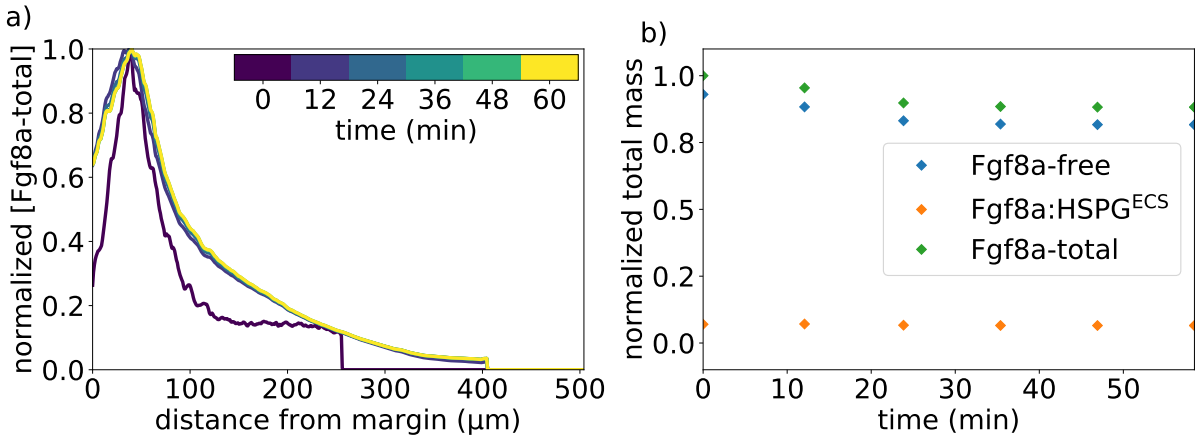

Figure 11: Simulated Fgf8a gradient using optimized parameters (Tab. 1) with experimental profile as initial condition. (a) Normalized AV concentration profiles of Fgf8a-total at different simulated times (color bar). All profiles are normalized by their respective maximum xz-plane-averaged concentration. The experimental profile used as initial condition is shown in dark purple (time 0). Simulated profiles reach a steady state within 12 min. (b) Normalized total mass of two Fgf8a fractions Fgf8a : HSPG^{ECS} and Fgf8a-free, along with their sum (Fgf8a-total). This set of parameters maintains a constant total Fgf8a mass and preserves the *in vivo* Fgf8a / Fgf8a : HSPG^{ECS} ratio of 93% / 7%).

3 Results

We use the model, simulation algorithm, and the parameter values described in Section 2 to study the emergence, maintenance, and robustness of the Fgf8a gradient in realistic ECS geometries of zebrafish embryos during epiboly. In particular, the computational model allows us to disentangle the influences of different molecular parameters and of the ECS geometry and shape. This enables testing for the sufficiency of an SDD mechanism of gradient formation and quantifying the sensitivity of the gradient to changes in the ECS geometry.

3.1 An SDD+HSPG-binding mechanism is sufficient to generate *de novo* Fgf8a gradients

We simulate *de novo* Fgf8a gradient formation in reconstructed zebrafish ECS geometries at ≈40, 60, and 75% epiboly. The simulations start from initial concentrations $[\mathrm{Fgf8a}] = [\mathrm{Fgf8a} : \mathrm{HSPG}^{\mathrm{ECS}}] = [\mathrm{Fgf8a} : \mathrm{HSPG}^{\mathrm{cellSurf}}] = [\mathrm{Fgf8a}_2 : \mathrm{HSPG}_2^{\mathrm{cellSurf}} : \mathrm{Fgfr}_2] = 0$ everywhere in the embryo to test whether an SDD+HSPG-binding mechanism is sufficient for the spontaneous emergence of an AV gradient.

The resulting concentration profiles and total mass over time at 60% epiboly are shown in Fig. 12. A steady state is reached at ≈30 minutes. The Fgf8a / Fgf8a : HSPG^{ECS} ratio remains almost constant (92.6% / 7.4%) throughout the simulated 60 minutes and very close to the *in vivo* measured ratio (93% / 7%). Interestingly the steady-state profile reached in the *de novo* simulation is similar to the steady-state profile when initializing with the experimental profile (Fig. 11), indicating an insensitivity of the steady state towards the initial condition.

Overall, the simulated steady-state profile is similar to the experimental profile (Fig. 9) but shows a slightly flatter gradient with longer range. A possible reason for this deviation is that

the *in vivo* profile has been averaged over a sub-volume of the embryo (yellow dotted lines in Fig. 9), whereas the simulated profile is computed across the entire ECS. Another reason could be modeling errors in the ECS geometry reconstruction or the simulation parameters. Indeed, the image segmentation tends to overestimate ECS thickness, reducing geometrical hindrance in the model compared to the real embryo and enabling Fgf8a to diffuse faster and further, which would explain the gradient flattening and increased decay length.

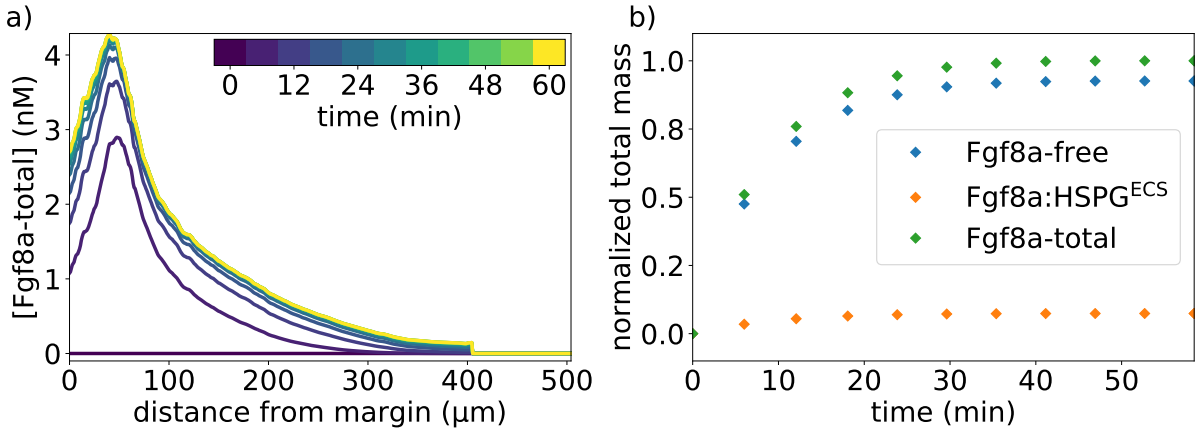

Figure 12: Simulated *de novo* Fgf8a gradient formation at 60 % epiboly. Initially, all Fgf8a concentrations were zero throughout the embryo. (a) Evolution of the emerging AV gradient profile of [Fgf8a − total] over time (color bar). The gradient reaches a steady state at ≈30 min. (b) The Fgf8a-free / Fgf8a : HSPG^{ECS} ratio remains almost constant (92.6% / 7.4%) and close to the experimentally measured values (93% / 7%) throughout the simulated 60 minutes.

We repeat the *de novo* gradient formation simulation in ECS geometries t ≈40 and ≈75 % epiboly. The results are shown in Fig. 13. Again, the simulated profiles are slightly flatter than the experimentally measured ones but are overall similar and show the same trend over developmental stages. Also, in the model, propagation lengths increase as epiboly progresses, probably due to a widening of the source band.

Interestingly, in addition to the AV gradient, the simulation also reproduces the DV gradient observed *in vivo* at 75% epiboly (see Supplementary Note S2, Suppl. Figs. S2 and S3). Since, in the model, the rates of all sources, sinks, and HSPG binding are invariant along the DV axis, this gradient can be interpreted as a consequence of ECS geometry asymmetry. In addition to this sufficient geometric asymmetry, earlier patterning events have been proposed to contribute to DV gradient formation [35, 89].

Taken together, these results show that the SDD+HSPG-binding mechanism modeled here is sufficient to cause the spontaneous emergence of AV and DV gradients in zebrafish embryo ECS geometries during epiboly. The mechanism also maintains the experimentally measured Fgf8a population fractions and explains the gradient evolution across epiboly stages.

3.2 Fgf8a normalized gradients are robust to changes in rate constants but sensitive to changes in ECS geometry

Factors such as temperature and DNA distribution can cause fluctuations in gene-expression levels and therefore reaction rates. Gradient robustness is the capacity to buffer the effect

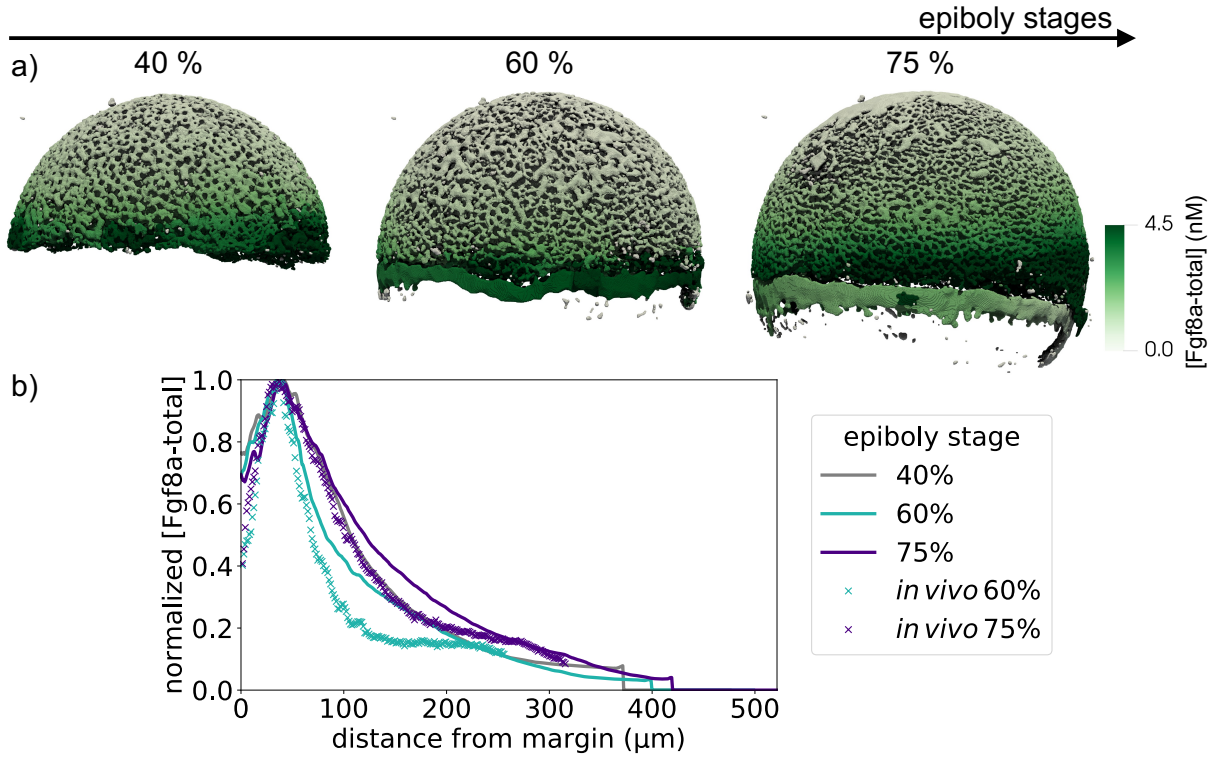

Figure 13: Simulated *de novo* Fgf8a gradient formation at 40, 60, and 75 % epiboly. (a) Visualization of the simulated Fgf8a-total concentrations in the ECS geometries at the respective stages. Initially, all Fgf8a concentrations were zero throughout the embryo. (b) Simulated (lines) and experimentally measured (symbols) AV profiles at different stages (colors, inset legend). Experimental profiles were only available at 60 and 75% epiboly. Simulated profiles are computed at $t = 60$ min.

of such fluctuations and is important to ensure that tissues develop correctly over a range of environmental conditions. Using our model in ECS geometries at 60% epiboly, we quantify how the rates of sources, sinks, HSPG binding, and diffusion influence the gradient profile. In addition, we study the impact of ECS geometry on the gradient.

The normalized gradient profile is robust against changes in source and sink rates

Morphogen gradients are surprisingly robust against changes in the source rate [28, 29, 65, 123]. To test whether our model reproduces this robustness, we simulate *de-novo* Fgf8a gradient formation for different k_{source}, keeping all other parameters fixed, until a steady state is reached at $t_{\max} = 60\,\text{min}$. The resulting AV gradient profiles in Supplementary Fig. S7a show that higher k_{source} lead to higher overall concentration levels, an expected consequence of increased morphogen secretion. However, normalizing by each profile's maximum concentration, as also done in experimental measurements, reveals that the gradient shape is almost invariant across 4 orders of magnitude in k_{source} (see Fig. 15a). Compared to the baseline $k_{\text{source}} = 0.1\,\text{nM s}^{-1}$, the gradient becomes only slightly flatter when decreasing k_{source} and slightly steeper when increasing k_{source}. The deviations are, however, very small.

This shows that the mechanisms modeled here are sufficient to explain the experimentally observed gradient robustness [28, 29, 65, 123]. In our simulations, the normalized Fgf8a AV gradient is robust to source-rate changes across 4 orders of magnitude, from $10^{-3} \ldots 10$. A possible explanation for this robustness is that the sink term scales with the morphogen concentration, thereby buffering the effects of variations in the production.

For the sink rate, *in-vivo* observations suggest that the gradient is not robust. It has been shown that modulating Fgf8a endocytosis in live zebrafish embryos makes normalized gradients shallower when inhibiting endocytosis and steeper when upregulating endocytosis [122]. We test the behavior of our model by changing $k_{\text{internalize}}$ while keeping all other parameters unchanged. The resulting gradient profiles in Fig. S7b suggest that decreasing $k_{\text{internalize}}$ leads to higher concentration levels, which is an expected consequence of reduced morphogen degradation. Normalizing the profiles, however, it can again be seen in Fig. 15b that the gradient shape is almost unaffected by changing $k_{\text{internalize}}$ across 4 orders of magnitude. A significant difference can only be seen within 50 µm from the margin, where the gradient becomes steeper for smaller $k_{\text{internalize}}$ than the baseline $k_{\text{internalize}} = 9 \cdot 10^{-3}\,\text{s}^{-1}$ but only slightly flatter for $k_{\text{internalize}}$ larger than baseline.

The simulation does therefore not explain the experimentally observed sensitivity of the gradient to endocytosis rates. The gradient flattening observed *in vivo* is therefore not caused by the molecular mechanisms modeled here. Instead, we speculate that it could be caused by side effects of a dominant-negative mutation of Dynamin, a GTPase that pinches off endocytic vesicles from the plasma membrane. Changes in Dynamin function are therefore not specific to Fgf8a endocytosis and may affect other feedback loops and downstream signaling cascades, too.

In conclusion, the simulation results show that an SDD+HSPG mechanism is sufficient for generating gradients whose normalized profile is robust to changes in k_{source} and $k_{\text{internalize}}$ across 4 orders of magnitude. This robustness does, however, not transfer to the absolute concentration gradient whose overall levels increase for increasing k_{source} and decreasing $k_{\text{internalize}}$.

Slower diffusion leads to steeper and shorter gradients

Next, we quantify gradient robustness against changes in morphogen diffusion. We simulate *de-novo* gradient formation using different diffusion coefficients of Fgf8a-free. The results are shown in Figs. S7c (absolute values) and 15c (normalized). Compared to the baseline diffusivity of $D_{\mathrm{Fgf8a}} = 55\,\mu\mathrm{m}^2\mathrm{s}^{-1}$, lower diffusion coefficients result in steeper gradients and shorter propagation lengths with narrower, higher peaks at the source. Increasing the diffusion coefficient leads to gradient flattening, longer propagation, and lower peak concentration.

This shows that the steady-state profile of the morphogen gradient depends on the morphogen diffusion coefficient. The dependence is much stronger than for the source and sink rates, where a 10,000-fold variation led to smaller changes in the gradient than a five-fold change of the diffusion constant. Faster diffusing morphogens can propagate further and have longer signaling ranges in the embryo, whereas slower diffusing morphogens maintain higher concentrations near the source and act more locally. This suggests that gradient formation could more generally be influenced by any factor hindering or promoting morphogen diffusion. This includes the geometric tortuosity of the diffusion space and HSPG binding.

To test the influence of HSPG binding on gradient formation, we simulate *de-novo* gradient formation for different $[\mathrm{HSPG}^{\mathrm{ECS}}]$ and $[\mathrm{HSPG}^{\mathrm{cellSurf}}]$. As shown in Fig. 15d, higher HSPG concentrations lead to gradients that are considerably steeper with shorter propagation lengths. Decreasing HSPG concentrations 10-fold below the baseline flattens the gradient. HSPG therefore acts on the gradient by modulating the effective diffusivity through transient matrix binding.

Flatter gradients for lower HSPG concentrations are in agreement with *in vivo* HepI-injection experiments. HepI is an enzyme that cleaves the HS side chains of HSPG, reducing the slow-diffusing Fgf8a fraction, thereby causing a shallower gradient [40, 122] as measured by FCS and shown in Fig. 14. HepI injection also increased the overall Fgf8a concentration in the ECS, which has been explained by Fgf8a dissociating from cell-surface HSPGs [40]. Our simulations reproduce this observation, showing higher Fgf8a peak concentrations at lower HSPG concentrations (see Fig. S7d).

Interestingly, decreasing HSPG concentrations below $[\mathrm{HSPG}^{\mathrm{ECS}}] = 40\,\mathrm{nM}$ and $[\mathrm{HSPG}^{\mathrm{cellSurf}}] = 100\,\mathrm{nM}$ does not further flatten the gradient. Even when setting all HSPG concentrations to zero and modeling gradient formation by an SDD mechanism, the same profile emerges as for $[\mathrm{HSPG}^{\mathrm{ECS}}] = 40\,\mathrm{nM}$ and $[\mathrm{HSPG}^{\mathrm{cellSurf}}] = 100\,\mathrm{nM}$ (see coinciding lines in Fig. 15d). This means that a minimal HSPG concentration is required to have a relevant effect on the gradient. This makes sense as below the baseline, the freely diffusing Fgf8a fraction constitutes $> 92\,\%$ of the total Fgf8a, dominating the gradient profile. This also shows that under the current modeling assumptions, an SDD mechanism is sufficient for the spontaneous formation and maintenance of some gradient, which is, however, flatter than the baseline and the *in vivo* gradient.

Both *in vivo* and *in silico*, $\mathrm{HSPG}^{\mathrm{cellSurf}}$ is involved in receptor binding and endocytosis of Fgf8a. Decreasing $[\mathrm{HSPG}^{\mathrm{cellSurf}}]$ thus also decreases sink fluxes. While changing the sink rate $k_{\mathrm{internalize}}$ did not affect the simulated gradient profile (Fig. 15), reducing the effective sink flux does.

Concluding, the present results show that morphogen gradients are sensitive to changes in morphogen diffusivity. Both reducing the molecular diffusion coefficient and the diffusive hindrance by HSPG binding have a similar effect, leading to steeper gradients with shorter

range and higher peak near the source. This is in agreement with previous 1D models showing that lower diffusion coefficients lead to steeper and shorter gradients [117] and with *in vivo* experiments showing that HSPG binding is crucial for maintaining high concentrations near the source and for restricting gradient propagation lengths [40].

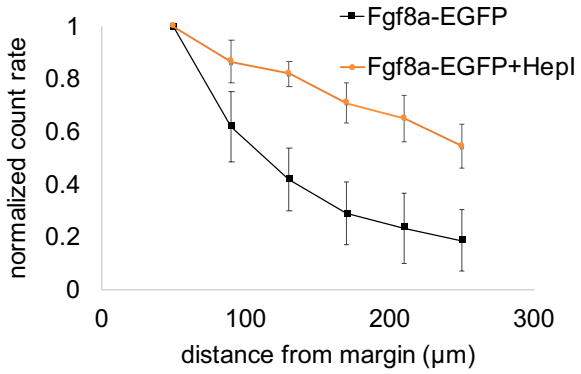

Figure 14: FCS count rates of Fgf8a without (black squares) and with (orange circles) HepI injection. The Fgf8a gradient of HepI-injected embryos is shallower. Figure reproduced with permission from Harish et al. [40] *to do: ask journal for permission.*

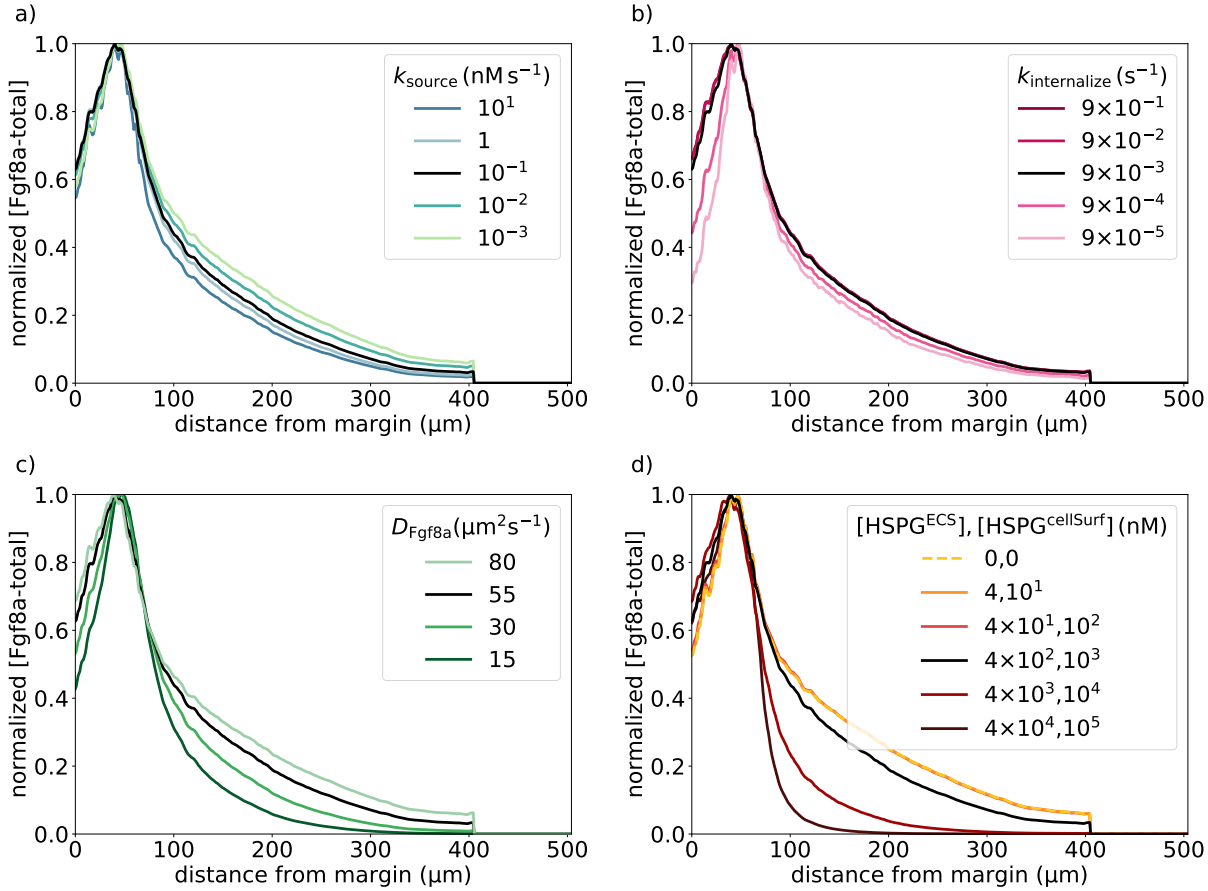

Figure 15: Sensitivity of simulated steady-state Fgf8a gradients to variations in the model parameters. The gradient shows remarkable robustness against changes in source (a) and sink rates (b) over four orders of magnitude (color, inset legend). Changes in the effective diffusivity, by changing either the molecular diffusion coefficient of Fgf8a (c) or HSPG concentrations (d), strongly affect the gradient. The higher HSPG binding and the smaller the diffusion coefficient, the steeper and shorter the gradient. The baseline gradient (Section 3.1) is shown as a solid black line in all panels. All profiles are normalized by their respective maximum xz-plane-averaged concentration. Profiles are shown at $t = 60$ min.

Tortuous ECS geometries stabilize Fgf8a gradients

The effect of decreasing HSPG concentrations is much smaller than when increasing them (Fig. 15d). Indeed, the gradient remains almost unchanged when reducing [$\mathrm{HSPG}^{\mathrm{ECS}}$] or [$\mathrm{HSPG}^{\mathrm{cellSurf}}$] by more than 10-fold. This suggests that the diffusive hindrance from HSPG binding is dominated by the tortuosity of the ECS geometry. This is consistent with HSPG being mostly localized near cell surfaces, mirroring the ECS geometry.

We use our realistic 3D ECS geometry model to quantify the effect of diffusive tortuosity on Fgf8a gradients. For this, we perturb the modeled ECS geometry and quantify the influence of these perturbations on simulated Fgf8a gradients. Such perturbations are straightforward in the numerical description of the ECS as a signed-distance function. Changing the surface level-set from the standard $\phi_{\mathrm{ECS}} = 0$ to other values uniformly changes the ECS tube diameters and thus the ECS density, connectivity, and volume.

We vary the geometry in steps of h from $\phi_{\mathrm{ECS}} = 3h$ (thinner ECS, higher tortuosity) down to $\phi_{\mathrm{ECS}} = -1h$ (thicker ECS, lower tortuosity) in comparison with the baseline $\phi_{\mathrm{ECS}} = 0$. The unit h is the grid spacing, i.e., twice the pixel size of the light-sheet microscopy images. Examples of resulting perturbed geometries are shown in Fig. 16a for $\phi_{\mathrm{ECS}} = -1h$ and $\phi_{\mathrm{ECS}} = 3h$. For these perturbed geometries, we compute steady-state Fgf8a gradient profiles, keeping all model parameters at their default values as given in Table 1.

The resulting absolute concentration profiles in Fig. 16b show that the thinner the ECS tubes, the more elevated the peak near the source, the steeper the gradients, and the shorter the range. The steeper, shorter gradients for higher ECS tortuosity are also confirmed in the normalized profiles (Fig. 16c). This shows that morphogen gradients are sensitive to ECS geometry and that geometric hindrance is sufficient to tune morphogen propagation lengths.

Thickening the ECS tubes by only $1h$ leads to negligible Fgf8a concentrations ($< 0.007\,\mathrm{nM}$) and a flat profile, shown in Fig. 16b. In the normalized profile, a peak at the source becomes apparent with a small peak concentration of $0.001\,\mathrm{nM}$. This amounts to $\approx$10 times the secreted concentration per simulation time step, showing that this peak can likely be attributed to instantly secreted Fgf8a, partly immobilized at the cell surface of secretion as $\mathrm{Fgf8a} : \mathrm{HSPG}^{\mathrm{cellSurf}}$ and $\mathrm{Fgf8a}_2 : \mathrm{HSPG}_2^{\mathrm{cellSurf}} : \mathrm{Fgfr}_2$. Away from the immediate source region, concentrations are zero and no gradient exists.

The absence of a gradient, in this case, can be explained as follows: The lower ECS tortuosity enables the morphogen to quickly diffuse away from the source and distribute throughout the target tissue, where it is degraded. In addition, the effective source flux is reduced as the surface area between ECS and deep cells is reduced by thickening the tubes. This is not balanced by the—for the same reason—lower effective sink flux. This shows that under the current modeling assumption of restricting the source to the deep-cell surfaces, increasing ECS thickness by $1h$ compared to the baseline results in a tortuosity insufficient to generate and maintain a gradient.

Taken together, these results show that the tortuous ECS geometry plays an important role in establishing and maintaining robust morphogen gradients. The geometric tortuosity regulates source peak height, gradient steepness, and propagation length. In geometries of insufficient tortuosity, gradients cannot be maintained. Regulating gradient formation and maintenance, therefore, involves adjusting extracellular HSPG concentrations and ECS tortuosity to the morphogen diffusion coefficient. The embryo can thus control the morphogen gradient by tuning

HSPG secretion and the shape of the interstitial space, e.g., by regulating cell adhesion and tissue rigidity [69, 82]. The present results suggest that the ECS tortuosity is tuned to just the minimum required to support long-range gradients, as already reducing it by one grid unit causes the gradient to vanish.

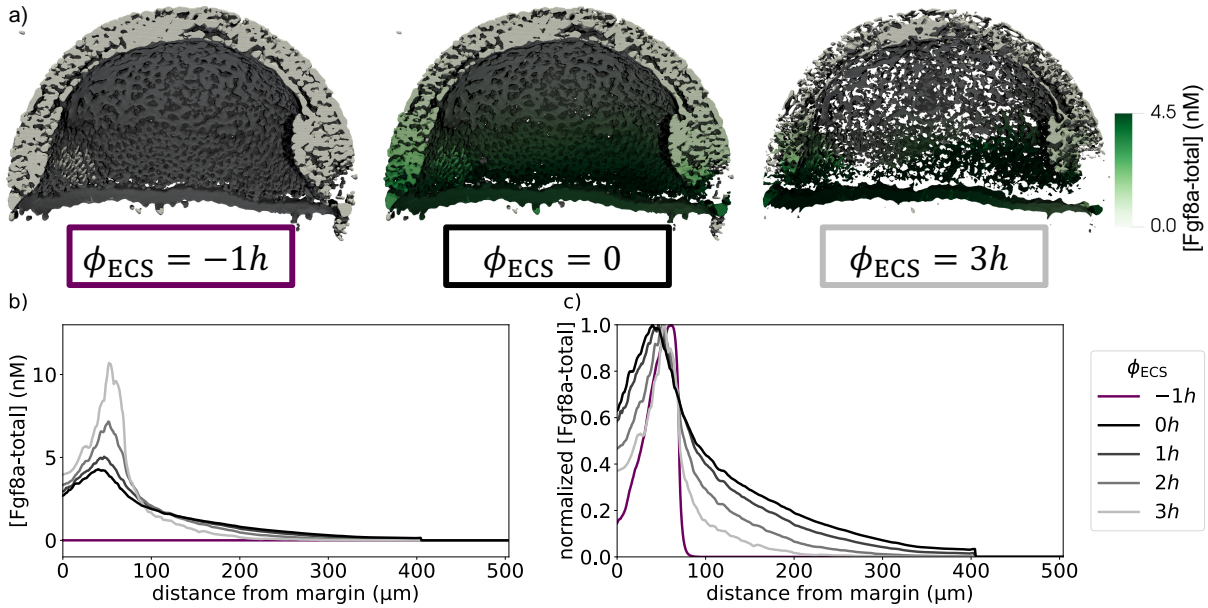

Figure 16: Fgf8a gradients are sensitive to ECS geometry. To test how ECS tortuosity influences Fgf8a gradients, we simulated *de-novo* gradient formation for different ECS geometries. (a) Clipped visualizations of the baseline ECS geometry (center) and two perturbed versions (left, right) with simulated Fgf8a concentrations overlaid in green, scaled to $[\mathrm{Fgf8a-total}]_{\mathrm{max}} = 4.5\,\mathrm{nM}$ (color bar). The ECS tube thickness is perturbed by changing the boundary location along ϕ_{ECS}, i.e., shifting down by one grid spacing h (2 pixels) to obtain thicker tubes and increasing by $3h$ to obtain thinner tubes. (b) Absolute AV concentration profiles at $t = 60$ minutes. Colors correspond to different geometries (inset legend). Compared to the baseline geometry (solid black line), decreasing ECS tube sizes limits Fgf8a propagation lengths and leads to a steeper gradient with a higher peak (lines shades of gray). Increasing the tube sizes and imposing sources and sinks only at the surfaces of the remaining cells causes the gradient to vanish (violet line). (c) The same profiles normalized to their respective maximum concentration values.

3.3 Porous-media characteristics of the ECS regulate gradient shape

So far, the results show that Fgf8a AV gradients are robust to changes in source and sink rates when simulated in realistic ECS geometries but sensitive to changes in the ECS geometry. Since the gradients are also sensitive to changes in the molecular diffusion constant and in transient HSPG binding, this suggests that diffusive hindrance may be a core mechanism in morphogen gradient emergence, maintenance, and robustness. Diffusive hindrance is a core concept of transport in porous media [3, 8, 12, 27, 30, 36, 91, 97, 98, 105, 115]. In the present system, diffusive hindrance results from the joint effect of geometric tortuosity, transient HSPG binding in the ECS and at the cell surfaces, receptor complex formation, and the finite molecular diffusion constant of the morphogen. In this sense, the ECS geometry, with its extracellular HSPG, effectively acts as a porous medium regulating Fgf8a gradient shape.

Our model resolves the porous medium explicitly by resolving geometry and binding reactions at the "pore scale". We test to what extent Fgf8a gradient shape can be explained by an effective porous medium. For this, we compare simulations in fully resolved ECS geometries with simulations in upscaled homogenizations [14, 45, 56]. In these homogenizations, the geometry is simplified to a spherical shell filled with a uniform porous material (see Fig. 17). This porous material models the coarse-grained effect of ECS geometry and diffusive hindrance without explicitly resolving them. In this simplified model, surface reactions and diffusive tortuosity are represented by uniformly distributed effective volume rates.

We obtain the simplified shell geometry by extracting the outer surfaces of our ECS geometry model at 60% epiboly, removing all internal cell surfaces. Using this shell model, we upscale the porous media characteristics of the ECS. In the upscaled model, the source is uniformly distributed within a deep-cell band at the blastoderm margin with the same width as in the fully resolved geometry model (70 µm), as shown in Fig. 17a.

We first quantify the effect of HSPG binding by simulating Fgf8a gradient formation by an SDD mechanism without HSPG binding but with Fgf8a degradation at rate k_{decay} in the entire shell. Using this homogenized model, we simulate *de-novo* gradient formation with the parameters given in Table 1 until a steady state is reached at $t = 60\,\mathrm{min}$. The normalized gradient profiles in Fig. 17d show that the gradient in the spherical shell geometry emerging from an SDD mechanism without HSPG (orange dashed line) does not reproduce the baseline gradient (black line). The gradient in the spherical shell is shallower with a longer propagation length and lacks the zonation near the margin. The latter is because in the coarse-grained model, the marginal region is fused with the shell, whereas in the real geometry, the margin is only weakly connected to the rest of the ECS. The flatness and long range can be explained by missing diffusive hindrance from HSPG and Fgfr binding and ECS tortuosity.

To upscale diffusive hindrance by HSPG binding and complex formation, we assume uniformly distributed $\mathrm{HSPG}^{\mathrm{ECS}}$ and $\mathrm{HSPG}^{\mathrm{cellSurf}}$ in the entire shell and receptor-mediated endocytosis throughout the DCL (see Fig. 17b). Figure 17d shows that *de-novo* gradient formation in the spherical shell with upscaled HSPG binding and receptor-mediated endocytosis leads to a steeper and shorter gradient (dark-green line) than with an SDD mechanism alone. This gradient is, however, still shallower than the baseline and lacks the zonation near the source. Despite these differences, a gradient does emerge in the shell. The diffusive hindrance provided by HSPG binding and receptor-complex formation in the entire volume of this geometry is stronger than in the baseline ECS geometry, where these effects are restricted to the cell surfaces.

The effect of geometric hindrance can be upscaled using the diffusive tortuosity τ_{d} of the ECS geometry, as defined in Eq. (S1), Supplementary Note S5. Using the fully resolved ECS geometry model, we numerically compute $\tau_{\mathrm{d}} = 2.5$ on average across the entire ECS, as detailed in Supplementary Note S5. This factor describes how strongly the ECS geometry alone hinders Fgf8a diffusion. Since our geometry model likely over-estimated the thickness of ECS structures, we expect the real τ_{d} to be even larger.

Simulating gradient formation in the spherical shell with upscaled diffusion coefficient $\tilde{D}_{\mathrm{Fgf8a}} = D_{\mathrm{Fgf8a}}/\tau_{\mathrm{d}} = 22\,\mu\mathrm{m}^2\mathrm{s}^{-1}$ indeed recovers gradient steepness and range (see Fig. 16d, green line). The geometric zonation effect near the source, however, is still not reproduced, as this local effect cannot be captured by an averaged tissue-wide factor.

In summary, these results show that the ECS effectively acts as a porous medium when

modulating morphogen gradient shape. In this, geometric tortuosity acts in concert with matrix and receptor binding to create the required diffusive hindrance. Hindrance from matrix binding alone cannot account for the correct gradient slope. The effective geometric hindrance, as represented by the upscaled tortuosity, restores the global gradient shape apart from local zonation effects. This shows that the porous-media characteristics of the ECS geometry are sufficient to explain morphogen gradient shape.

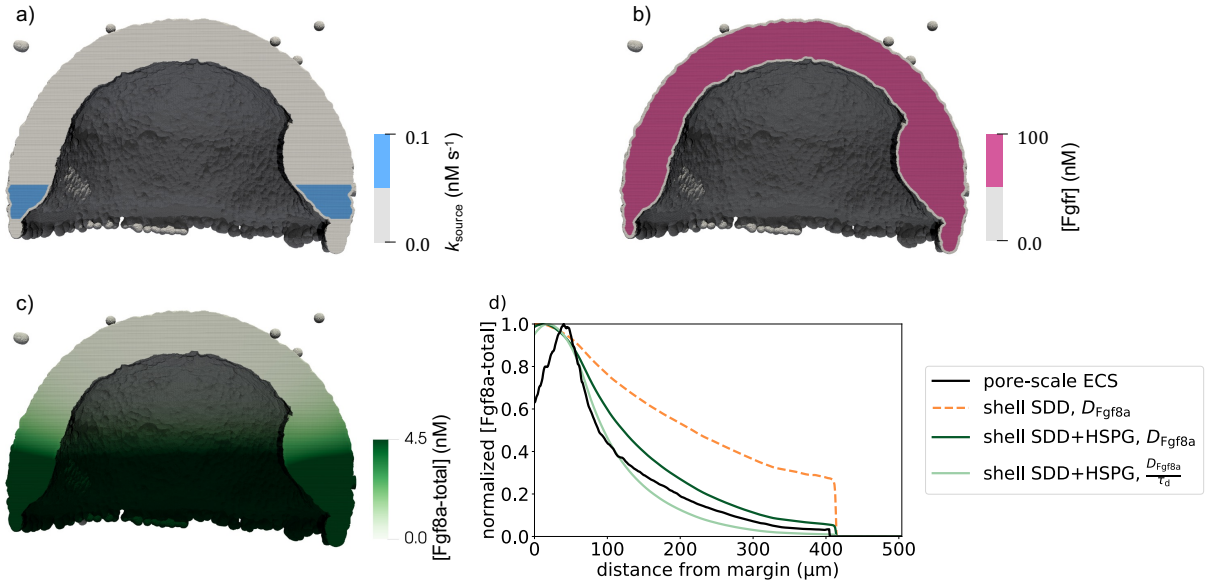

Figure 17: Upscaling porous-media ECS characteristics in the shell geometry. Clipped simulation visualization of (a) the source in a 70 µm DCL band at the margin, (b) the uniformly distributed sink ([Fgfr]) in the DCL, and (c) the Fgf8a gradient at $t = 60$ minutes (concentration color bar) using the parameters from Table 1. (d) Modeling the ECS geometry as a spherical shell without HSPG leads to a longer, flatter gradient (orange dashed line) compared to the baseline of the pore-scale model (black line). Gradient steepness and range are partly recovered by upscaling HSPG binding by uniformly distributed HSPG^{ECS} and $\text{HSPG}^{\text{cellSurf}}$, and it is fully recovered when further upscaling the tortuosity by an effective diffusion coefficient using τ_{d} (as defined in Supplementary Note S5). This does, however, not apply to local geometry effects such as the zonation near the source. AV profiles are reported at $t = 60.0$ min.

4 Discussion and Conclusions

Combining image-based three-dimensional geometry modeling with geometry-adaptive numerical simulation methods enabled reconstituting morphogen gradient emergence and maintenance *in silico* in realistic embryo geometries with fully resolved interstitial space, surface, and bulk biochemistry. We reconstructed pore-scale extracellular space (ECS) geometries of zebrafish embryos during epiboly from light-sheet microscopy videos and numerically solved the governing equations of Fgf8a gradient formation in those geometries. The simulations were validated against *in vivo* fluorescence intensity profiles and fluorescence correlation spectroscopy (FCS) measurements. This enabled quantifying the robustness of the Fgf8a morphogen gradient with respect to individual molecular parameters, such as diffusion constants and source/sink rates, and to the ECS geometry itself. We found that the Fgf8a gradient along the AV axis of the

embryo is robust against changes in the morphogen source and sink rates but sensitive to perturbations of the ECS geometry, suggesting that the geometry plays an important role in gradient shaping and maintenance.

We also showed that the *in vivo* measured gradient profile can be explained by a source-diffusion-degradation (SDD) mechanism with additional heparan-sulfate proteoglycan (HSPG) binding in the extracellular matrix. Indeed, this mechanism was sufficient for spontaneous *de novo* formation of realistic and temporally stable animal-vegetal (AV) Fgf8a gradients in the fully resolved 3D ECS geometry. This indicates that the "SDD+HSPG+ECS" mechanism proposed here is sufficient to explain the emergence, scaling, maintenance, and robustness of morphogen gradients.

A key challenge when modeling morphogen gradient formation is that several molecular parameters are unknown. In order to improve the predictive power of our model, we fixed as many parameters as possible to experimentally measured or literature values. For the remaining three parameters, the Fgf8a production rate and the HSPG concentrations in the ECS, we performed a computational search, identifying parameters for which the model maintained the free versus HSPG-bound Fgf8a ratio observed *in vivo*. Using these parameters, the model was able to reproduce *de novo* emergence of the Fgf8a AV gradient in ECS geometries at ≈40, 60, and 75% epiboly. In all cases, the gradients reached a steady state after about 30 minutes. In addition to the AV gradient, the model reproduced the weaker DV gradient as observed *in vivo* at 75% epiboly, showing that asymmetries in the ECS geometry are sufficient to explain this secondary gradient.

We next tested how the ECS geometry contributes to gradient robustness against changing rates of sources, sinks, and HSPG binding. We found that the normalized gradient was remarkably robust against variations in source and sink rates across four orders of magnitude. In contrast, the gradient profile was sensitive to changes in the Fgf8a diffusion constant and the HSPG concentrations, as well as to perturbations of the ECS geometry. All of these three factors create diffusive hindrance for the morphogen.

A slower molecular diffusion coefficient trivially hinders morphogen diffusion. HSPG contributes to diffusive hindrance by transiently binding the morphogen in the ECS and sequestering it to cell surfaces. The embryo can thus control gradient steepness and range by tuning heparan-sulfate affinity and by modulating the HSPG secretion rate. In addition, the tortuosity of the ECS geometry provides a significant contribution to diffusive hindrance and seems to be tuned to just the minimum required to support long-range gradients. ECS tortuosity can be controlled by the embryo by tuning cell density and adhesion. Cell adhesion is modulated, for example, during tissue fluidization of the central deep cells at the animal pole during the onset of doming [82]. During fluidization, cells detach, increasing the interstitial space [69, 82]. Hence, by regulating tissue rigidity, embryos can influence tortuosity-mediated hindrance of the morphogen. The aggregate diffusive hindrance is key to preserving high morphogen concentrations near the source and regulating gradient steepness and range.

Diffusive hindrance is a core characteristic of porous media. We thus suggest that the ECS in the developing embryo effectively acts as a porous medium toward the morphogen gradient. Indeed, we were able to restore the long-range gradient profile by coarse-graining (i.e., computational upscaling) the average porous-media characteristics of the ECS geometry into a spherical shell. This showed that morphogen gradients are regulated by porous media

characteristics of embryo geometry.

Coarse-grained average porous media characteristics, however, were not able to account for the zonation effect near the blastoderm margin, where reduced ECS pore connectivity leads to an offset concentration peak. This effect was reproduced in the fully resolved realistic ECS geometry, whereas it was naturally lost in an average upscaling. This means that although effective porous media characteristics of the ECS govern the long-range gradient shape and range, local features may still intricately depend on the geometric details of the diffusion space.

This dependence on local geometric detail also implies that our results are sensitive to image-segmentation and geometry-modeling errors. While the image-based geometry used here was sufficiently realistic to demonstrate the pore-scale effects of geometry and explain the experimental observation, it likely underestimated real ECS tortuosity. The model could be refined in the future by enhancing image acquisition and segmentation. In addition, the model could be improved by further refining the parameter values. Machine-learning approaches that mimic the simulation, such as neural network surrogate models [61], could be used in the future to accelerate parameter exploration.

The present model also neglects flows in the ECS due to tissue growth and cell motion. We modeled the geometry as static at each epiboly stage, assuming that diffusive transport in the ECS is significantly faster than the time scale of tissue deformation. This is an approximation, as the real embryo geometry varies continuously over time. Although dilution effects are likely negligible during epiboly, as the ECS volume does not change (see Supplementary Note S4), cell movement has been proposed to contribute to gradient formation by additional advective transport [61]. Quantifying the contributions from advection and deformation would require explicitly modeling tissue dynamics. Tracking the ECS geometry over time to derive continuous deformation maps requires image data with a higher time resolution than the light-sheet microscopy video used here. Once available, such deformation maps could be included in our model by correspondingly evolving the level-set function [10] and simulating the induced flows in the ECS [103]. Such simulations would also enable studying how morphogen gradients scale across different tissue sizes during growth [18, 34].

Ultimately, tissue growth and size could emerge from the simulated physics of the model rather than being imposed from image data. This would involve computationally predicting tissue deformation [19] from the hydrodynamics of the extracellular fluid and the active growth and motion of the cells within the morphogen gradient as a biphasic active poroelastic material [87] or an active gel [85, 104]. Velocity fields for advective morphogen transport could then be computed from the pressure gradients in the interstitial fluid, e.g., using Darcy's law for porous materials [87]. Such a model would then be able to, e.g., explain changing ECS geometries during tissue fluidization of the central deep cells at the onset of doming during zebrafish epiboly [82]. This could then be combined with Wnt signaling at the blastoderm margin, inhibiting cell detachment and maintaining stiff tissue mechanics [82]. Fully coupling morphogen gradient formation, geometry evolution, tissue mechanics, and hydrodynamics would constitute an important step towards understanding morphogenesis as a fully self-organized mechano-chemical process [58, 86].

In addition to tissue mechanics, it will be exciting to couple morphogen gradients to upstream and downstream signaling pathways. This could be achieved in the presented model by incorporating additional concentration fields and signaling reactions. These could be identified

from or validated against gene-expression [43] or spatial transcriptomics data [71, 72], e.g., from RNAscopes [116], single-molecule fluorescence *in-situ* hybridization (smFISH) [60], sequential fluorescence *in-situ* hybridization (seqFISH) [63], or single-cell RNA sequencing (scRNAseq) [41, 55] with tissue reference maps [1, 95]. Complementary to recent work that studied the relationship between spatial gene expression and tissue mechanics [39], our model could be extended to enable quantitative analyses of the relationship between spatial gene expression and morphogen gradients.

A model considering all four aspects—realistic 3D embryo geometry, chemical gradients, tissue mechanics, and gene expression—would enable a mechanistic understanding of morphogenesis as a self-organized mechano-chemical process and help guide *in vivo* experiments in developmental biology.

The present work provides a first step in this direction, considering realistic ECS and embryo geometry and providing a sufficient mechanism for morphogen gradient formation, maintenance, and robustness. We here focused on Fgf8a gradients in zebrafish embryos during epiboly. The presented modeling workflow and computer-simulation algorithm, however, is not limited to this specific case.

Beyond the case of zebrafish epiboly, many morphogen gradients form and act in complex-shaped diffusion spaces involving surface reactions such as secretion and endocytosis [73]. We have shown here that the geometry of the diffusion space can play an important role in shaping and stabilizing a morphogen gradient. We have also shown that, apart from local zonation effects, this is governed by porous-media characteristics of the tissue. Towards a morphogen gradient, a developing tissue thus acts as a porous medium whose physico-chemical and geometric characteristics regulate gradient dynamics.

The regulation of morphogen gradients by porous-media characteristics of the tissue may constitute a general principle. Morphogen gradients typically form within complex geometric environments and are subject to surface and bulk reactions. Diffusive hindrance from binding reactions and geometric tortuosity, the two key mechanisms identified here, are thus likely universal, albeit different molecules may play this role in different systems.

Data availability

The simulation software used in this work is available under the 3-clause BSD license and free of charge from `https://github.com/mosaic-group/openfpm`. We provide the specific code of this paper on `https://git.mpi-cbg.de/mosaic/reactiondiffusion_imagebased_porousmedia.git`.

Acknowledgments

We thank Dr. Nandu Gopan, Alejandra Foggia, and Dr. Johannes Pahlke (all Sbalzarini lab, CSBD Dresden) and Dr. Anastasia Solomatina (Leibniz-HKI Jena) for fruitful discussions and comments on the manuscript, and Dr. Pietro Incardona (University of Bonn) for help with the OpenFPM implementation of the simulation software.

References

[1] Kaia Achim et al. "High-throughput spatial mapping of single-cell RNA-seq data to tissue of origin". In: *Nature Biotechnology* 33.5 (2015), pp. 503–509. ISSN: 1087-0156. DOI: 10.1038/nbt.3209. URL: https://www.nature.com/articles/nbt.3209.

[2] Daniel Aguilar-Hidalgo et al. "Critical Point in Self-Organized Tissue Growth". In: *Physical Review Letters* 120.19 (2018), pp. 1–6. ISSN: 10797114. DOI: 10.1103/PhysRevLett.120.198102. arXiv: 1711.02021.

[3] Gustave E. Archie. "The electrical resistivity log as an aid in determining some reservoir characteristics". In: *Transactions of the AIME* 146.01 (1942), pp. 54–62. DOI: https://doi.org/10.2118/942054-G.

[4] Gyeong Hun Baeg and Norbert Perrimon. "Functional binding of secreted molecules to heparan sulfate proteoglycans in Drosophila". In: *Current Opinion in Cell Biology* 12.5 (2000), pp. 575–580. ISSN: 09550674. DOI: 10.1016/S0955-0674(00)00134-4. URL: https://linkinghub.elsevier.com/retrieve/pii/S0955067400001344.

[5] Sofia Barbieri et al. "Modeling protein dynamics in Caenorhabditis elegans embryos reveals that the PLK-1 gradient relies on weakly coupled reaction-diffusion mechanisms". In: *Proceedings of the National Academy of Sciences of the United States of America* 119.11 (2022), e2114205119. ISSN: 10916490. DOI: 10.1073/pnas.2114205119. URL: https://pnas.org/doi/full/10.1073/pnas.2114205119.

[6] Alexander M. Berezhkovskii, Mathieu Coppey, and Stanislav Y. Shvartsman. "Signaling gradients in cascades of two-state reaction-diffusion systems". In: *Proceedings of the National Academy of Sciences* 106.4 (2009), pp. 1087–1092. ISSN: 0027-8424. DOI: 10.1073/pnas.0811807106. URL: https://pnas.org/doi/full/10.1073/pnas.0811807106.

[7] Alexander M. Berezhkovskii, Christine Sample, and Stanislav Y. Shvartsman. "Formation of morphogen gradients: Local accumulation time". In: *Physical Review E* 83.5 (2011), p. 051906. ISSN: 1539-3755. DOI: 10.1103/PhysRevE.83.051906. URL: https://link.aps.org/doi/10.1103/PhysRevE.83.051906.

[8] Alexander M. Berezhkovskii, Vladimir Yu Zitserman, and Stanislav Y. Shvartsman. "Diffusivity in periodic arrays of spherical cavities". In: *The Journal of Chemical Physics* 118.15 (2003), pp. 7146–7147. ISSN: 0021-9606. DOI: 10.1063/1.1561615. URL: https://pubs.aip.org/jcp/article/118/15/7146/839815/Diffusivity-in-periodic-arrays-of-spherical.

[9] Stuart Berg et al. "ilastik: interactive machine learning for (bio)image analysis". In: *Nature Methods* (2019). ISSN: 1548-7105. DOI: 10.1038/s41592-019-0582-9. URL: https://doi.org/10.1038/s41592-019-0582-9.

[10] Michael Bergdorf and Petros Koumoutsakos. "A Lagrangian Particle-Wavelet Method". In: *Multiscale Modeling & Simulation* 5.3 (2006), pp. 980–995. ISSN: 1540-3459. DOI: 10.1137/060652877. URL: http://epubs.siam.org/doi/10.1137/060652877.

[11] Bernd Boehm et al. "The Role of Spatially Controlled Cell Proliferation in Limb Bud Morphogenesis". In: *PLoS Biology* 8.7 (2010). Ed. by Alfonso Martinez Arias, e1000420. ISSN: 1545-7885. DOI: 10.1371/journal.pbio.1000420. URL: https://dx.plos.org/10.1371/journal.pbio.1000420.

[12] M. P. Bohrer, Gary D. Patterson, and P. J. Carroll. "Hindered Diffusion of Dextran and Ficoll in Microporous Membranes". In: *Macromolecules* 17.6 (1984), pp. 1170–1173. ISSN: 15205835. DOI: 10.1021/ma00136a011.

[13] Bernard P. Boudreau. "The diffusive tortuosity of fine-grained unlithified sediments". In: *Geochimica et Cosmochimica Acta* 60.16 (1996), pp. 3139–3142. ISSN: 00167037. DOI: 10.1016/0016-7037(96)00158-5.

[14] Mohamed Khaled Bourbatache et al. "Homogenized model for diffusion and heterogeneous reaction in porous media: Numerical study and validation." In: *Applied Mathematical Modelling* 111 (2022), pp. 486–500. ISSN: 0307904X. DOI: 10.1016/j.apm.2022.07.001. URL: https://linkinghub.elsevier.com/retrieve/pii/S0307904X22003249.

[15] J. van Brakel and P. M. Heertjes. "Analysis of diffusion in macroporous media in terms of a porosity, a tortuosity and a constrictivity factor". In: *International Journal of Heat and Mass Transfer* 17.9 (1974), pp. 1093–1103. ISSN: 00179310. DOI: 10.1016/0017-9310(74)90190-2.

[16] Paul C Bressloff. "Morphogen gradient formation in partially absorbing media". In: *Physical Biology* 19.6 (2022), p. 066005. ISSN: 1478-3967. DOI: 10.1088/1478-3975/ac95ea. arXiv: 2209.07290. URL: https://iopscience.iop.org/article/10.1088/1478-3975/ac95ea%E2%80%93%E2%80%93%E2%80%93.

[17] Ashley E.E. Bruce. "Zebrafish epiboly: Spreading thin over the yolk". In: *Developmental Dynamics* 245.3 (2016), pp. 244–258. ISSN: 10588388. DOI: 10.1002/dvdy.24353. URL: https://onlinelibrary.wiley.com/doi/10.1002/dvdy.24353.

[18] Daniel Čapek and Patrick Müller. "Positional information and tissue scaling during development and regeneration". In: *Development* 146.24 (2019), dev177709. ISSN: 1477-9129. DOI: 10.1242/dev.177709. URL: https://doi.org/10.1242/dev.177709.

[19] Vito Conte, José J. Muñoz, and Mark Miodownik. "A 3D finite element model of ventral furrow invagination in the Drosophila melanogaster embryo". In: *Journal of the Mechanical Behavior of Biomedical Materials* 1.2 (2008), pp. 188–198. ISSN: 17516161. DOI: 10.1016/j.jmbbm.2007.10.002. URL: https://linkinghub.elsevier.com/retrieve/pii/S175161610700032X.

[20] Mathieu Coppey et al. "Modeling the bicoid gradient: Diffusion and reversible nuclear trapping of a stable protein". In: *Developmental Biology* 312.2 (2007), pp. 623–630. ISSN: 00121606. DOI: 10.1016/j.ydbio.2007.09.058. URL: https://linkinghub.elsevier.com/retrieve/pii/S001216060701411X.

[21] Marco Crialesi-Esposito et al. "FluTAS: A GPU-accelerated finite difference code for multiphase flows". In: *Computer Physics Communications* 284 (2022), p. 108602. ISSN: 00104655. DOI: 10.1016/j.cpc.2022.108602. arXiv: 2204.08834. URL: https://doi.org/10.1016/j.cpc.2022.108602.

[22] Arthur D. Lander, Qing Nie, and Frederic Y. M. Wan. "Spatially Distributed Morphogen Production and Morphogen Gradient Formation". In: *Mathematical Biosciences and Engineering* 2.2 (2005), pp. 239–262. ISSN: 1551-0018. DOI: 10.3934/mbe.2005.2.239. URL: http://www.aimspress.com/article/10.3934/mbe.2005.2.239.

[23] S. Dalessi, A. Neves, and S. Bergmann. "Modeling morphogen gradient formation from arbitrary realistically shaped sources". In: *Journal of Theoretical Biology* 294 (2011), pp. 130–138. ISSN: 00225193. DOI: 10.1016/j.jtbi.2011.10.014. URL: http://dx.doi.org/10.1016/j.jtbi.2011.10.014.

[24] Giovanni Dalmasso et al. "4D reconstruction of murine developmental trajectories using spherical harmonics". In: *Developmental Cell* 57.17 (2022), 2140–2150.e5. ISSN: 18781551. DOI: 10.1016/j.devcel.2022.08.005.

[25] J M P Q Delgado. "A Simple Experimental Technique to Measure Tortuosity in Packed Beds". In: *The Canadian Journal of Chemical Engineering* 84.6 (2006), pp. 651–655. DOI: https://doi.org/10.1002/cjce.5450840603. URL: https://onlinelibrary.wiley.com/doi/abs/10.1002/cjce.5450840603.

[26] Bruce W. Draper, David W. Stock, and Charles B. Kimmel. "Zebrafish fgf24 functions with fgf8 to promote posterior mesodermal development". In: *Development* 130.19 (2003), pp. 4639–4654. ISSN: 09501991. DOI: 10.1242/dev.00671. URL: https://journals.biologists.com/dev/article/130/19/4639/42074/Zebrafish-fgf24-functions-with-fgf8-to-promote.

[27] Ronald C. Dykhuizen and William H. Casey. "An analysis of solute diffusion in rocks". In: *Geochimica et Cosmochimica Acta* 53.11 (1989), pp. 2797–2805. ISSN: 00167037. DOI: 10.1016/0016-7037(89)90157-9.

[28] Avigdor Eldar, Ben-Zion Shilo, and Naama Barkai. "Elucidating mechanisms underlying robustness of morphogen gradients". In: *Current Opinion in Genetics & Development* 14.4 (2004), pp. 435–439. ISSN: 0959437X. DOI: 10.1016/j.gde.2004.06.009. URL: https://linkinghub.elsevier.com/retrieve/pii/S0959437X04000887.

[29] Avigdor Eldar et al. "Robustness of the BMP morphogen gradient in Drosophila embryonic patterning". In: *Nature* 419.6904 (2002), pp. 304–308. ISSN: 0028-0836. DOI: 10.1038/nature01061. URL: https://www.nature.com/articles/nature01061.

[30] Jean Matthieu Etancelin, Peter Moonen, and Philippe Poncet. "Improvement of remeshed Lagrangian methods for the simulation of dissolution processes at pore-scale". In: *Advances in Water Resources* 146 (2020), p. 103780. ISSN: 03091708. DOI: 10.1016/j.advwatres.2020.103780. URL: https://doi.org/10.1016/j.advwatres.2020.103780.

[31] J. A. Ferreira, G. Pena, and G. Romanazzi. "Anomalous diffusion in porous media". In: *Applied Mathematical Modelling* 40.3 (2016), pp. 1850–1862. ISSN: 0307904X. DOI: 10.1016/j.apm.2015.09.034.

[32] Renee J. Filion and Aleksander S. Popel. "A reaction-diffusion model of basic fibroblast growth factor interactions with cell surface receptors". In: *Annals of Biomedical Engineering* 32.5 (2004), pp. 645–663. ISSN: 00906964. DOI: 10.1023/B:ABME.0000030231.88326.78.

[33] Kimberly Forsten-Williams et al. "Control of Growth Factor Networks by Heparan Sulfate Proteoglycans". In: *Annals of Biomedical Engineering* 36.12 (2008), pp. 2134–2148. ISSN: 0090-6964. DOI: 10.1007/s10439-008-9575-z. URL: http://link.springer.com/10.1007/s10439-008-9575-z.

[34] Patrick Fried and Dagmar Iber. "Dynamic scaling of morphogen gradients on growing domains". In: *Nature Communications* 5.1 (2014), p. 5077. ISSN: 20411723. DOI: 10.1038/ncomms6077. URL: https://www.nature.com/articles/ncomms6077.

[35] Maximilian Fürthauer, C Thisse, and Bernard Thisse. "A role for FGF-8 in the dorsoventral patterning of the zebrafish gastrula." In: *Development (Cambridge, England)* 124.21 (1997), pp. 4253–64. ISSN: 0950-1991. DOI: 10.1242/dev.124.21.4253. URL: http://www.ncbi.nlm.nih.gov/pubmed/9334274.

[36] Behzad Ghanbarian et al. "Tortuosity in Porous Media: A Critical Review". In: *Soil Science Society of America Journal* 77.5 (2013), pp. 1461–1477. ISSN: 03615995. DOI: 10.2136/sssaj2012.0435.

[37] Thomas Gregor et al. "Stability and Nuclear Dynamics of the Bicoid Morphogen Gradient". In: *Cell* 130.1 (2007), pp. 141–152. ISSN: 00928674. DOI: 10.1016/j.cell.2007.05.026. URL: https://linkinghub.elsevier.com/retrieve/pii/S0092867407006630.

[38] Mansi Gupta et al. "Fine-tuning of Fgf8 morphogen gradient by heparan sulfate proteoglycans in the extracellular matrix". In: *bioRxiv* (2023). DOI: 10.1101/2023.11.02.565243. URL: https://www.biorxiv.org/content/early/2023/11/02/2023.11.02.565243.

[39] Adrien Hallou et al. "A computational pipeline for spatial mechano-transcriptomics". In: *bioRxiv* (2023), p. 2023.08.03.551894. DOI: 10.1101/2023.08.03.551894. URL: http://biorxiv.org/content/early/2023/08/05/2023.08.03.551894.abstract.

[40] Rohit Krishnan Harish et al. "Real-time monitoring of endogenous Fgf8a gradient attests to its role as a morphogen during zebrafish gastrulation". In: *Development* (2023), dev.201559. ISSN: 0950-1991. DOI: 10.1242/dev.201559. URL: https://doi.org/10.1242/dev.201559.

[41] Tamar Hashimshony et al. "CEL-Seq: Single-Cell RNA-Seq by Multiplexed Linear Amplification". In: *Cell Reports* 2.3 (2012), pp. 666–673. ISSN: 22111247. DOI: 10.1016/j.celrep.2012.08.003. URL: http://dx.doi.org/10.1016/j.celrep.2012.08.003.

[42] Ellen Margrethe Haugsten et al. "Different intracellular trafficking of FGF1 endocytosed by the four homologous FGF receptors." In: *Journal of cell science* 118.Pt 17 (2005), pp. 3869–81. ISSN: 0021-9533. DOI: 10.1242/jcs.02509. URL: http://www.ncbi.nlm.nih.gov/pubmed/16091423.

[43] Jacob Hecksher-Sørensen and James Sharpe. "3D confocal reconstruction of gene expression in mouse". In: *Mechanisms of Development* 100.1 (2001), pp. 59–63. ISSN: 09254773. DOI: 10.1016/S0925-4773(00)00508-6.

[44] Jingwei Huang et al. "Diffusion tortuosity in complex porous media from pore-scale numerical simulations". In: *Computers and Fluids* 183 (2019), pp. 66–74. ISSN: 00457930. DOI: 10.1016/j.compfluid.2019.03.018. URL: https://doi.org/10.1016/j.compfluid.2019.03.018.

[45] Laurène Hume and Philippe Poncet. "A velocity-vorticity method for highly viscous 3D flows with application to digital rock physics". In: *Journal of Computational Physics* 425 (2021), p. 109910. ISSN: 00219991. DOI: 10.1016/j.jcp.2020.109910. URL: https://linkinghub.elsevier.com/retrieve/pii/S0021999120306847.

[46] Jaroslav Icha et al. "Using light sheet fluorescence microscopy to image zebrafish eye development". In: *Journal of Visualized Experiments* 2016.110 (2016), pp. 1–21. ISSN: 1940087X. DOI: 10.3791/53966.

[47] Pietro Incardona, Tommaso Bianucci, and Ivo F. Sbalzarini. "Distributed Sparse Block Grids on GPUs". In: *High Performance Computing*. Ed. by Bradford L Chamberlain et al. Vol. 12728 LNCS. Cham: Springer International Publishing, 2021, pp. 272–290. ISBN: 978-3-030-78713-4. DOI: 10.1007/978-3-030-78713-4_15. URL: http://dx.doi.org/10.1007/978-3-030-78713-4%7B%5C_%7D15.

[48] Pietro Incardona et al. "A portable C++ library for memory and compute abstraction on multi-core CPUs and GPUs". In: *Concurrency and Computation: Practice and Experience* 35.25 (2023), e7870. ISSN: 1532-0626. DOI: 10.1002/cpe.7870. URL: https://doi.org/10.1002/cpe.7870.

[49] Pietro Incardona et al. "OpenFPM: A scalable open framework for particle and particle-mesh codes on parallel computers". In: *Computer Physics Communications* 241 (2019), pp. 155–177. ISSN: 00104655. DOI: 10.1016/j.cpc.2019.03.007. URL: https://linkinghub.elsevier.com/retrieve/pii/S0010465519300852.

[50] Md Saiful Islam and Tom Manzocchi. "A novel flow-based geometrical upscaling method to represent three-dimensional complex sub-seismic fault zone structures into a dynamic reservoir model". In: *Scientific Reports* 9.1 (2019), p. 5294. ISSN: 2045-2322. DOI: 10.1038/s41598-019-41723-y. URL: https://www.nature.com/articles/s41598-019-41723-y.

[51] Satya P. Jammy, Christian T. Jacobs, and Neil D. Sandham. "Performance evaluation of explicit finite difference algorithms with varying amounts of computational and memory intensity". In: *Journal of Computational Science* 36 (2019), p. 100565. ISSN: 18777503. DOI: 10.1016/j.jocs.2016.10.015. URL: http://dx.doi.org/10.1016/j.jocs.2016.10.015.

[52] Anna Kicheva et al. "Kinetics of morphogen gradient formation". In: *Science* 315.5811 (2007), pp. 521–525. ISSN: 00368075. DOI: 10.1126/science.1135774. URL: https://www.science.org/doi/10.1126/science.1135774.

[53] Goo-Young Kim et al. "HtrA1 is a novel antagonist controlling fibroblast growth factor (FGF) signaling via cleavage of FGF8." In: *Molecular and cellular biology* 32.21 (2012), pp. 4482–92. ISSN: 1098-5549. DOI: 10.1128/MCB.00872-12. URL: http://www.ncbi.nlm.nih.gov/pubmed/22949504.

[54] Andrei Y. Kobitski et al. "An ensemble-averaged, cell density-based digital model of zebrafish embryo development derived from light-sheet microscopy data with single-cell resolution." In: *Scientific reports* 5 (2015), p. 8601. ISSN: 2045-2322. DOI: 10.1038/srep08601. URL: http://www.ncbi.nlm.nih.gov/pubmed/25712513.

[55] Merlin Lange et al. "Zebrahub – Multimodal Zebrafish Developmental Atlas Reveals the State Transition Dynamics of Late Vertebrate Pluripotent Axial Progenitors". In: *bioRxiv* (2023), p. 2023.03.06.531398. DOI: https://doi.org/10.1101/2023.03.06.531398. URL: http://biorxiv.org/content/early/2023/03/07/2023.03.06.531398.abstract.

[56] Tien Dung Le et al. "A spectral approach for homogenization of diffusion and heterogeneous reaction in porous media". In: *Applied Mathematical Modelling* 104 (2022), pp. 666–681. ISSN: 0307904X. DOI: 10.1016/j.apm.2021.12.017. URL: https://doi.org/10.1016/j.apm.2021.12.017.

[57] Jinzhi Lei and You Song. "Mathematical Model of the Formation of Morphogen Gradients Through Membrane-Associated Non-receptors". In: *Bulletin of Mathematical Biology* 72.4 (2010), pp. 805–829. ISSN: 0092-8240. DOI: 10.1007/s11538-009-9470-2. URL: http://link.springer.com/10.1007/s11538-009-9470-2.

[58] Pierre-François Lenne et al. "Roadmap for the multiscale coupling of biochemical and mechanical signals during development". In: *Physical Biology* 18.4 (2021), p. 041501. ISSN: 1478-3967. DOI: 10.1088/1478-3975/abd0db. URL: https://iopscience.iop.org/article/10.1088/1478-3975/abd0db.

[59] Gaja Lesnicar-Pucko et al. "Cellular mechanisms of chick limb bud morphogenesis". In: *bioRxiv* (2020), p. 2020.09.10.292359. URL: https://www.biorxiv.org/content/10.1101/2020.09.10.292359v1%7B%5C%%7D0Ahttps://www.biorxiv.org/content/10.1101/2020.09.10.292359v1.abstract.

[60] Jeffrey M. Levsky and Robert H. Singer. "Fluorescence in situ hybridization: past, present and future". In: *Journal of Cell Science* 116.14 (2003), pp. 2833–2838. ISSN: 1477-9137. DOI: 10.1242/jcs.00633. URL: https://journals.biologists.com/jcs/article/116/14/2833/27272/Fluorescence-in-situ-hybridization-past-present.

[61] Linlin Li et al. "Determining the role of advection in patterning by bone morphogenetic proteins through neural network model-based acceleration of a 3D finite element model of the zebrafish embryo". In: *Frontiers in Systems Biology* 2.October (2022), pp. 1–

12. ISSN: 2674-0702. DOI: 10.3389/fsysb.2022.983372. URL: https://www.frontiersin.org/articles/10.3389/fsysb.2022.983372/full.

[62] Linlin Li et al. "Evaluation of BMP-mediated patterning in a 3D mathematical model of the zebrafish blastula embryo." In: *Journal of mathematical biology* 80.1-2 (2020), pp. 505–520. ISSN: 1432-1416. DOI: 10.1007/s00285-019-01449-x. URL: http://www.ncbi.nlm.nih.gov/pubmed/31773243.

[63] T. Lohoff et al. "Integration of spatial and single-cell transcriptomic data elucidates mouse organogenesis." In: *Nature biotechnology* 40.1 (2022), pp. 74–85. ISSN: 1546-1696. DOI: 10.1038/s41587-021-01006-2. URL: http://www.ncbi.nlm.nih.gov/pubmed/34489600.

[64] Y. Lou, Q. Nie, and F. Y. M. Wan. "Nonlinear Eigenvalue Problems in the Stability Analysis of Morphogen Gradients". In: *Studies in Applied Mathematics* 113.2 (2004), pp. 183–215. ISSN: 0022-2526. DOI: 10.1111/j.1467-9590.2004.01530.x. URL: https://onlinelibrary.wiley.com/doi/10.1111/j.1467-9590.2004.01530.x.

[65] Aasakiran Madamanchi, Mary C. Mullins, and David M. Umulis. "Diversity and robustness of bone morphogenetic protein pattern formation". In: *Development* 148.7 (2021). ISSN: 0950-1991. DOI: 10.1242/dev.192344. URL: https://journals.biologists.com/dev/article/148/7/dev192344/238078/Diversity-and-robustness-of-bone-morphogenetic.

[66] Luciano Marcon et al. "A Computational Clonal Analysis of the Developing Mouse Limb Bud". In: *PLoS Computational Biology* 7.2 (2011). Ed. by Stanislav Shvartsman, e1001071. ISSN: 1553-7358. DOI: 10.1371/journal.pcbi.1001071. URL: https://dx.plos.org/10.1371/journal.pcbi.1001071.

[67] Denis Menshykau et al. "Image-based modeling of kidney branching morphogenesis reveals GDNF-RET based Turing-type mechanism and pattern-modulating WNT11 feedback". In: *Nature Communications* 10.1 (2019), p. 239. ISSN: 2041-1723. DOI: 10.1038/s41467-018-08212-8. URL: https://www.nature.com/articles/s41467-018-08212-8.

[68] Luis Felipe Millan Claro et al. "THREE-DIMENSIONAL COMPUTATIONAL MODEL OF EARLY UPPER LIMB DEVELOPMENT". In: *Journal of Mechanics in Medicine and Biology* 22.1 (2022). ISSN: 02195194. DOI: 10.1142/S021951942250004X. URL: https://www.worldscientific.com/doi/10.1142/S021951942250004X.

[69] Alessandro Mongera et al. "A fluid-to-solid jamming transition underlies vertebrate body axis elongation". In: *Nature* 561.7723 (2018), pp. 401–405. ISSN: 14764687. DOI: 10.1038/s41586-018-0479-2. URL: http://dx.doi.org/10.1038/s41586-018-0479-2.

[70] Anne M. Moon and Mario R. Capecchi. "Fgf8 is required for outgrowth and patterning of the limbs". In: *Nature Genetics* 26.4 (2000), pp. 455–459. ISSN: 10614036. DOI: 10.1038/82601. URL: https://www.nature.com/articles/ng1200%7B%5C_%7D455.

[71] Andreas E. Moor and Shalev Itzkovitz. "Spatial transcriptomics: paving the way for tissue-level systems biology". In: *Current Opinion in Biotechnology* 46 (2017), pp. 126–133. ISSN: 09581669. DOI: 10.1016/j.copbio.2017.02.004. URL: http://dx.doi.org/10.1016/j.copbio.2017.02.004.

[72] Lambda Moses and Lior Pachter. "Museum of spatial transcriptomics". In: *Nature Methods* 19.5 (2022), pp. 534–546. ISSN: 1548-7091. DOI: 10.1038/s41592-022-01409-2. URL: https://www.nature.com/articles/s41592-022-01409-2.

[73] Patrick Müller et al. "Morphogen transport". In: *Development* 140.8 (2013), pp. 1621–1638. ISSN: 1477-9129. DOI: 10.1242/dev.083519. URL: https://journals.biologists.com/dev/article/140/8/1621/46025/Morphogen-transport.

[74] Michael D. Multerer et al. "Simulation of Morphogen and Tissue Dynamics". In: *Methods in Molecular Biology* 1863 (2018), pp. 223–250. ISSN: 10643745. DOI: 10.1007/978-1-4939-8772-6_13. arXiv: 1806.04138.

[75] Stuart A Newman et al. "Multiscale models for vertebrate limb development." In: *Current topics in developmental biology* 81.07 (2008), pp. 311–40. ISSN: 0070-2153. DOI: 10.1016/S0070-2153(07)81011-8. URL: http://www.ncbi.nlm.nih.gov/pubmed/18023733.

[76] Charles Nicholson. "Diffusion and related transport mechanisms in brain tissue". In: *Reports on Progress in Physics* 64.7 (2001), pp. 815–884. ISSN: 0034-4885. DOI: 10.1088/0034-4885/64/7/202. URL: https://iopscience.iop.org/article/10.1088/0034-4885/64/7/202.

[77] Charles Nicholson and Eva Syková. "Extracellular space structure revealed by diffusion analysis." In: *Trends in neurosciences* 21.5 (1998), pp. 207–15. ISSN: 0166-2236. DOI: 10.1016/s0166-2236(98)01261-2. URL: http://www.ncbi.nlm.nih.gov/pubmed/9610885.

[78] David M. Ornitz and Nobuyuki Itoh. "The fibroblast growth factor signaling pathway". In: *Wiley Interdisciplinary Reviews: Developmental Biology* 4.3 (2015), pp. 215–266. ISSN: 17597692. DOI: 10.1002/wdev.176. URL: https://onlinelibrary.wiley.com/doi/10.1002/wdev.176.

[79] Stanley Osher and James A. Sethian. "Fronts propagating with curvature-dependent speed: Algorithms based on Hamilton-Jacobi formulations". In: *Journal of Computational Physics* (1988). ISSN: 10902716. DOI: 10.1016/0021-9991(88)90002-2.

[80] Satoshi Ota et al. "FGF receptor gene expression and its regulation by FGF signaling during early zebrafish development." In: *Genesis (New York, N.Y. : 2000)* 48.12 (2010), pp. 707–16. ISSN: 1526-968X. DOI: 10.1002/dvg.20682. URL: http://www.ncbi.nlm.nih.gov/pubmed/20960516.

[81] Danping Peng et al. "A PDE-Based Fast Local Level Set Method". In: *Journal of Computational Physics* 155.2 (1999), pp. 410–438. ISSN: 00219991. DOI: 10.1006/jcph.1999.6345.

[82] Nicoletta I. Petridou et al. "Fluidization-mediated tissue spreading by mitotic cell rounding and non-canonical Wnt signalling". In: *Nature Cell Biology* 21.2 (2019), pp. 169–178. ISSN: 1465-7392. DOI: 10.1038/s41556-018-0247-4. URL: http://dx.doi.org/10.1038/s41556-018-0247-4.

[83] Stephan Preibisch et al. "Efficient Bayesian-based multiview deconvolution". In: *Nature Methods* 11.6 (2014), pp. 645–648. ISSN: 1548-7091. DOI: 10.1038/nmeth.2929. URL: https://www.nature.com/articles/nmeth.2929.

[84] Stephan Preibisch et al. "Software for bead-based registration of selective plane illumination microscopy data". In: *Nature Methods* 7.6 (2010), pp. 418–419. ISSN: 1548-7091. DOI: 10.1038/nmeth0610-418. URL: https://www.nature.com/articles/nmeth0610-418.

[85] J. Prost, F. Jülicher, and J-F. Joanny. "Active gel physics". In: *Nature Physics* 11.2 (2015), pp. 111–117. ISSN: 1745-2473. DOI: 10.1038/nphys3224. URL: https://www.nature.com/articles/nphys3224.

[86] Alireza Ramezani et al. "A multiscale chemical-mechanical model predicts impact of morphogen spreading on tissue growth". In: *npj Systems Biology and Applications* 9.1 (2023), p. 16. ISSN: 2056-7189. DOI: 10.1038/s41540-023-00278-5. URL: https://www.nature.com/articles/s41540-023-00278-5.

[87] Pierre Recho, Adrien Hallou, and Edouard Hannezo. "Theory of mechanochemical patterning in biphasic biological tissues". In: *Proceedings of the National Academy of Sciences* 116.12 (2019), pp. 5344–5349. ISSN: 0027-8424. DOI: 10.1073/pnas.1813255116. arXiv: 1811.12242. URL: https://pnas.org/doi/full/10.1073/pnas.1813255116.

[88] Gregory T. Reeves et al. "Quantitative Models of Developmental Pattern Formation". In: *Developmental Cell* 11.3 (2006), pp. 289–300. ISSN: 15345807. DOI: 10.1016/j.devcel.2006.08.006. URL: https://linkinghub.elsevier.com/retrieve/pii/S1534580706003522.

[89] Frank Reifers et al. "Fgf8 is mutated in zebrafish acerebellar (ace) mutants and is required for maintenance of midbrain-hindbrain boundary development and somitogenesis." In: *Development (Cambridge, England)* 125.13 (1998), pp. 2381–95. ISSN: 0950-1991. DOI: 10.1242/dev.125.13.2381. URL: http://www.ncbi.nlm.nih.gov/pubmed/9609821.

[90] Jonas Ries et al. "Modular scanning FCS quantifies receptor-ligand interactions in living multicellular organisms". In: *Nature methods* 6.9 (2009), pp. 643–645.

[91] Hector Rusinque and Gunther Brenner. "Mass transport in porous media at the micro- and nanoscale: A novel method to model hindered diffusion". In: *Microporous and Mesoporous Materials* 280 (2019), pp. 157–165. ISSN: 13871811. DOI: 10.1016/j.micromeso.2019.01.037. URL: https://doi.org/10.1016/j.micromeso.2019.01.037.

[92] O. Saksela et al. "Endothelial cell-derived heparan sulfate binds basic fibroblast growth factor and protects it from proteolytic degradation." In: *The Journal of cell biology* 107.2 (1988), pp. 743–51. ISSN: 0021-9525. DOI: 10.1083/jcb.107.2.743. URL: http://www.ncbi.nlm.nih.gov/pubmed/2971068%20http://www.pubmedcentral.nih.gov/articlerender.fcgi?artid=PMC2115214.

[93] Christine Sample and Stanislav Y. Shvartsman. "Multiscale modeling of diffusion in the early Drosophila embryo". In: *Proceedings of the National Academy of Sciences* 107.22 (2010), pp. 10092–10096. ISSN: 0027-8424. DOI: 10.1073/pnas.1001139107. URL: https://pnas.org/doi/full/10.1073/pnas.1001139107.

[94] Stephane Sarrazin, William C. Lamanna, and Jeffrey D. Esko. "Heparan Sulfate Proteoglycans". In: *Cold Spring Harbor Perspectives in Biology* 3.7 (2011), a004952–a004952. ISSN: 1943-0264. DOI: 10.1101/cshperspect.a004952. URL: http://cshperspectives.cshlp.org/lookup/doi/10.1101/cshperspect.a004952.

[95] Rahul Satija et al. "Spatial reconstruction of single-cell gene expression data". In: *Nature Biotechnology* 33.5 (2015), pp. 495–502. ISSN: 1087-0156. DOI: 10.1038/nbt.3192. URL: https://www.nature.com/articles/nbt.3192.

[96] Charles N Satterfield and Thomas Kilgore Sherwood. *The role of diffusion in catalysis*. Addison-Wesley publishing company, 1963.

[97] Charles N. Satterfield, Clark K. Colton, and Wayne H. Pitcher. "Restricted diffusion in liquids within fine pores". In: *AIChE Journal* 19.3 (1973), pp. 628–635. ISSN: 0001-1541. DOI: 10.1002/aic.690190332. URL: https://aiche.onlinelibrary.wiley.com/doi/10.1002/aic.690190332.

[98] Ivo F. Sbalzarini et al. "Effects of Organelle Shape on Fluorescence Recovery after Photobleaching". In: *Biophysical Journal* 89.3 (2005), pp. 1482–1492. ISSN: 0006-3495. DOI: https://doi.org/10.1529/biophysj.104.057885. URL: https://www.sciencedirect.com/science/article/pii/S000634950572796X.

[99] Johannes Schindelin et al. "Fiji: an open-source platform for biological-image analysis." In: *Nature methods* 9.7 (2012), pp. 676–82. ISSN: 1548-7105. DOI: 10.1038/nmeth.2019. URL: https://www.nature.com/articles/nmeth.2019.

[100] Joseph Schlessinger et al. "Crystal structure of a ternary FGF-FGFR-heparin complex reveals a dual role for heparin in FGFR binding and dimerization." In: *Molecular cell* 6.3 (2000), pp. 743–50. ISSN: 1097-2765. DOI: 10.1016/s1097-2765(00)00073-3. URL: http://www.ncbi.nlm.nih.gov/pubmed/11030354.

[101] Steffen Scholpp and Michael Brand. "Endocytosis Controls Spreading and Effective Signaling Range of Fgf8 Protein". In: *Current Biology* 14.20 (2004), pp. 1834–1841. ISSN: 09609822. DOI: 10.1016/j.cub.2004.09.084. URL: https://www.sciencedirect.com/science/article/pii/S0960982204007481.

[102] Steffen Scholpp, Claudia Lohs, and Michael Brand. "Engrailed and Fgf8 act synergistically to maintain the boundary between diencephalon and mesencephalon". In: *Development* 130.20 (2003), pp. 4881–4893. ISSN: 09501991. DOI: 10.1242/dev.00683. URL: https://journals.biologists.com/dev/article/130/20/4881/52223/Engrailed-and-Fgf8-act-synergistically-to-maintain.

[103] Lennart J. Schulze, Sachin K. T. Veettill, and Ivo F. Sbalzarini. "A high-order fully Lagrangian particle level-set method for dynamic surfaces". In: *arXiv* (2023). DOI: https://doi.org/10.48550/arXiv.2306.07986. arXiv: 2306.07986. URL: http://arxiv.org/abs/2306.07986.

[104] Anis Senoussi, Jean-Christophe Galas, and André Estevez-Torres. "Programmed mechanochemical coupling in reaction-diffusion active matter". In: *Science Advances* 7.51 (2021), pp. 1–10. ISSN: 2375-2548. DOI: 10.1126/sciadv.abi9865. URL: https://www.science.org/doi/10.1126/sciadv.abi9865.

[105] Lihua Shen and Zhangxin Chen. "Critical review of the impact of tortuosity on diffusion". In: *Chemical Engineering Science* 62.14 (2007), pp. 3748–3755. ISSN: 00092509. DOI: 10.1016/j.ces.2007.03.041.

[106] J. M. Smith. *Chemical Engineering Kinetics*. Vol. 2nd Editio. McGraw-Hill, New York, 1970, p. 414.

[107] Anastasia Solomatina et al. "Design centering enables robustness screening of pattern formation models". In: *Bioinformatics* 38.Supplement_2 (2022), pp. ii134–ii140. ISSN: 1367-4803. DOI: 10.1093/bioinformatics/btac480. URL: https://academic.oup.com/bioinformatics/article/38/Supplement%7B%5C_%7D2/ii134/6702014.

[108] Gizette V. Sperinde and Matthew A. Nugent. "Mechanisms of fibroblast growth factor 2 intracellular processing: a kinetic analysis of the role of heparan sulfate proteoglycans." In: *Biochemistry* 39.13 (2000), pp. 3788–96. ISSN: 0006-2960. DOI: 10.1021/bi992243d. URL: http://www.ncbi.nlm.nih.gov/pubmed/10736179.

[109] Kristina S. Stapornwongkul and Jean Paul Vincent. "Generation of extracellular morphogen gradients: the case for diffusion". In: *Nature Reviews Genetics* 22.6 (2021), pp. 393–411. ISSN: 14710064. DOI: 10.1038/s41576-021-00342-y. URL: http://dx.doi.org/10.1038/s41576-021-00342-y.

[110] Justina Stark and Ivo F. Sbalzarini. "An open-source pipeline for solving continuous reaction–diffusion models in image-based geometries of porous media". In: *Journal of Computational Science* 72 (2023), p. 102118. ISSN: 18777503. DOI: 10.1016/j.jocs.2023.102118. URL: https://linkinghub.elsevier.com/retrieve/pii/S1877750323001783.

[111] Mark Sussman and Emad Fatemi. "An Efficient, Interface-Preserving Level Set Redistancing Algorithm and Its Application to Interfacial Incompressible Fluid Flow". In: *SIAM Journal on Scientific Computing* 20.4 (1999), pp. 1165–1191. ISSN: 1064-8275. DOI: 10.1137/S1064827596298245. URL: http://epubs.siam.org/doi/10.1137/S1064827596298245.

[112] David M. Umulis and Hans G. Othmer. "The importance of geometry in mathematical models of developing systems". In: *Current Opinion in Genetics and Development* 22.6 (2012), pp. 547–552. ISSN: 0959437X. DOI: 10.1016/j.gde.2012.09.007. URL: http://dx.doi.org/10.1016/j.gde.2012.09.007.

[113] Francisco J Valdés-Parada, Didier Lasseux, and Stephen Whitaker. "Diffusion and Heterogeneous Reaction in Porous Media: The Macroscale Model Revisited". In: *International Journal of Chemical Reactor Engineering*. International Journal of Chemical Reactor Engineering 15.6 (2017). DOI: doi:10.1515/ijcre-2017-0151. URL: https://doi.org/10.1515/ijcre-2017-0151.

[114] Pauli Virtanen et al. "SciPy 1.0: fundamental algorithms for scientific computing in Python". In: *Nature Methods* 17.3 (2020), pp. 261–272. ISSN: 15487105. DOI: 10.1038/s41592-019-0686-2. arXiv: 1907.10121.

[115] N. Wakao and J. M. Smith. "Diffusion in catalyst pellets". In: *Chemical Engineering Science* 17.11 (1962), pp. 825–834. ISSN: 00092509. DOI: 10.1016/0009-2509(62)87015-8.

[116] Fay Wang et al. "RNAscope: a novel in situ RNA analysis platform for formalin-fixed, paraffin-embedded tissues." In: *The Journal of molecular diagnostics : JMD* 14.1 (2012), pp. 22–9. ISSN: 1943-7811. DOI: 10.1016/j.jmoldx.2011.08.002. URL: https://linkinghub.elsevier.com/retrieve/pii/S1525157811002571%20http://www.ncbi.nlm.nih.gov/pubmed/22166544%20http://www.pubmedcentral.nih.gov/articlerender.fcgi?artid=PMC3338343.

[117] Ortrud Wartlick, Anna Kicheva, and Marcos González-Gaitán. "Morphogen gradient formation." In: *Cold Spring Harbor perspectives in biology* 1.3 (2009). ISSN: 19430264. DOI: 10.1101/cshperspect.a001255.

[118] Paul B. Weisz. "Diffusion and chemical transformation." In: *Science (New York, N.Y.)* 179.4072 (1973), pp. 433–40. ISSN: 0036-8075. DOI: 10.1126/science.179.4072.433. URL: http://www.ncbi.nlm.nih.gov/pubmed/4705341.

[119] Dong Yan and Xinhua Lin. "Shaping Morphogen Gradients by Proteoglycans". In: *Cold Spring Harbor Perspectives in Biology* 1.3 (2009), a002493–a002493. ISSN: 1943-0264. DOI: 10.1101/cshperspect.a002493. URL: http://cshperspectives.cshlp.org/lookup/doi/10.1101/cshperspect.a002493.

[120] Jinmeng Yang, Shuqin Liu, and Hongwei Yin. "Local accumulation times of morphogen gradient with tissue growth". In: *International Journal of Modern Physics B* 33.25 (2019), p. 1950293. ISSN: 0217-9792. DOI: 10.1142/S021797921950293X. URL: https://www.worldscientific.com/doi/abs/10.1142/S021797921950293X.

[121] Chuang-Chao Ye et al. "Accelerating CFD simulation with high order finite difference method on curvilinear coordinates for modern GPU clusters". In: *Advances in Aerodynamics* 4.1 (2022), p. 7. ISSN: 2524-6992. DOI: 10.1186/s42774-021-00098-3. URL: https://doi.org/10.1186/s42774-021-00098-3.

[122] Shuizi Rachel Yu et al. "Fgf8 morphogen gradient forms by a source-sink mechanism with freely diffusing molecules". In: *Nature* 461.7263 (2009), pp. 533–536. ISSN: 0028-0836. DOI: 10.1038/nature08391. URL: https://www.nature.com/articles/nature08391.

[123] Zhechun Zhang et al. "Mouse embryo geometry drives formation of robust signaling gradients through receptor localization". In: *Nature Communications* 10.1 (2019). ISSN: 20411723. DOI: 10.1038/s41467-019-12533-7. URL: http://dx.doi.org/10.1038/s41467-019-12533-7.